Characterizing SASI- and Convection-Dominated Core-Collapse Supernova Explosions in Two Dimensions

Rodrigo Fernández[1,2,3], Bernhard Müller[4], Thierry Foglizzo[5], Hans-Thomas Janka[4]

[1] *Institute for Advanced Study, Princeton, NJ 08540, USA*
[2] *Department of Physics, University of California, Berkeley, CA 94720, USA*
[3] *Department of Astronomy & Theoretical Astrophysics Center, University of California, Berkeley, CA 94720, USA*
[4] *Max-Planck-Institut für Astrophysik, Karl-Schwarzschild-Str. 1, D-85748 Garching, Germany*
[5] *Laboratoire AIM, CEA/DSM-CNRS-Université Paris Diderot, IRFU/Service d'Astrophysique, CEA-Saclay F-91191, France*

ABSTRACT

The success of the neutrino mechanism of core-collapse supernovae relies on the supporting action of two hydrodynamic instabilities: neutrino-driven convection and the Standing Accretion Shock Instability (SASI). Depending on the structure of the stellar progenitor, each of these instabilities can dominate the evolution of the gain region prior to the onset of explosion, with implications for the ensuing asymmetries. Here we examine the flow dynamics in the neighborhood of explosion by means of parametric two-dimensional, time-dependent hydrodynamic simulations for which the linear stability properties are well understood. We find that systems for which the convection parameter χ is sub-critical (SASI-dominated) develop explosions once large-scale, high-entropy bubbles are able to survive for several SASI oscillation cycles. These long-lived structures are seeded by the SASI during shock expansions. Finite-amplitude initial perturbations do not alter this outcome qualitatively, though they can lead to significant differences in explosion times. Supercritical systems (convection-dominated) also explode by developing large-scale bubbles, though the formation of these structures is due to buoyant activity. Non-exploding systems achieve a quasi-steady state in which the time-averaged flow adjusts itself to be convectively sub-critical. We characterize the turbulent flow using a spherical Fourier-Bessel decomposition, identifying the relevant scalings and connecting temporal and spatial components. Finally, we verify the applicability of these principles on the general relativistic, radiation-hydrodynamic simulations of Müller, Janka, & Heger (2012), and discuss implications for the three-dimensional case.

Key words: hydrodynamics — instabilities – neutrinos – nuclear reactions, nucleosynthesis, abundances — shock waves – supernovae: general

1 INTRODUCTION

In the neutrino mechanism of core-collapse supernovae, a small fraction of the energy emitted in neutrinos by the forming neutron star is deposited in a layer behind the stalled accretion shock, powering its final expansion (Bethe & Wilson 1985). Extensive theoretical work over the last two decades has led to a consensus on the failure of this mechanism in spherically symmetric systems, except for the very lightest stellar progenitors (see, e.g., Janka 2012 for a recent review).

Successful neutrino-driven explosions require additional assistance by non-spherical hydrodynamic instabilities that increase the efficiency of neutrino energy deposition. This phenomenon has been observed in numerous two-dimensional (e.g., Herant et al. 1994; Burrows et al.

1995; Janka & Müller 1996; Mezzacappa et al. 1998; Scheck et al. 2006; Ohnishi et al. 2006; Buras et al. 2006; Burrows et al. 2007; Murphy & Burrows 2008; Ott et al. 2008; Marek & Janka 2009; Suwa et al. 2010; Müller et al. 2012; Couch 2013b) as well as three-dimensional (e.g., Iwakami et al. 2008; Nordhaus et al. 2010; Hanke et al. 2012; Burrows et al. 2012; Müller et al. 2012; Takiwaki et al. 2012; Ott et al. 2013; Couch 2013a; Dolence et al. 2013; Hanke et al. 2013) core-collapse simulations of various levels of sophistication. In addition to assisting the onset of explosion, these instabilities can contribute to the generation of pulsar kicks (Scheck et al. 2006; Nordhaus et al. 2010; Wongwathanarat et al. 2010), the spin-up of the forming neutron star (Fryer & Young 2007; Blondin & Mezzacappa 2007; Blondin & Shaw 2007; Fernández 2010) and the seeding of late-time

asymmetries (Kifonidis et al. 2006; Hammer et al. 2010; Wongwathanarat et al. 2013).

The shock-neutrinosphere cavity is unstable to *convection* driven by the energy deposition from neutrinos emitted in deeper layers (e.g., Bethe 1990). This process generates kinetic energy on spatial scales comparable to or smaller than the size of the neutrino heating region. Work by Blondin et al. (2003) and Blondin & Mezzacappa (2006) isolated a distinct, global oscillatory instability of the standing accretion shock that operates independent of neutrino heating, the so-called Standing Accretion Shock Instability (SASI). The driving mechanism involves an unstable cycle of advected and acoustic perturbations trapped within the shock-neutrinosphere cavity (Foglizzo et al. 2007; Foglizzo 2009; Guilet & Foglizzo 2012). The most unstable modes of the SASI reside on the largest spatial scales. Convection and the SASI are easily distinguishable in the linear regime, but their effects become intertwined in the non-linear turbulent flow that follows the stalling of the bounce supernova shock (e.g., Scheck et al. 2008).

Recent three-dimensional studies of core-collapse supernova hydrodynamics have found that large-scale oscillation modes of the shock attain smaller amplitudes than in two dimensions (Nordhaus et al. 2010; Wongwathanarat et al. 2010; Hanke et al. 2012; Takiwaki et al. 2012; Murphy et al. 2013). This has been interpreted as a consequence of the different behavior of turbulence in two- and three-dimensions (Hanke et al. 2012), and has led to the suggestion that the SASI may play a secondary role in the explosion mechanism, if it arises at all (Burrows et al. 2012; Burrows 2013). These models have largely focused on a small sample of stellar progenitors, however, and in many cases do not include physical effects that are favorable for the growth of the SASI (Janka et al. 2012).

Müller et al. (2012) followed the collapse and bounce of 8.1 and $27 M_\odot$ progenitors using a two-dimensional, general relativistic hydrodynamic code with energy dependent neutrino transport, finding that differences in progenitor structure lead to very different paths to explosion. In particular, the $27 M_\odot$ progenitor evolution is such that the SASI dominates the dynamics throughout the pre-explosion phase. Three-dimensional simulations of the same progenitor, with similar neutrino treatment, display episodic SASI activity, though a successful explosion is not yet obtained (Hanke et al. 2013). Ott et al. (2013) evolved the same $27 M_\odot$ progenitor with a more approximate neutrino prescription and a higher level of numerical perturbations, initially finding smaller SASI amplitudes than Müller et al. (2012) and Hanke et al. (2013), though later confirming SASI activity (C. Ott 2013, private communication). The lack of the same level of numerical perturbations in the Müller et al. (2012) models could mean that convection dominance instead of SASI dominance is dependent not only on the progenitor structure, but also on the details of the initial conditions.

It is the purpose of this paper to investigate some of these issues involving the interplay of SASI and convection, and the implications for successful explosions. In particular, we address the following questions: (1) Is there a fundamental difference between the transition to explosion in SASI- and convection-dominated models? (2) Can finite amplitude perturbations, generated in, e.g., multi-dimensional stellar progenitors (e.g., Arnett & Meakin 2011), tilt the balance in favor of convection in situations that would otherwise be SASI-dominated? (3) Does the SASI play any discernible role in convection-dominated systems? (4) Are there systematic trends in models close to an explosion that shed insight into the operation of each instability?

Our approach is experimental, employing hydrodynamic simulations that model neutrino source terms, the equation of state, and gravity in a parametric way (e.g., Fernández & Thompson 2009a). This setup has the advantage that its linear stability properties are well understood (Fernández & Thompson 2009b), allowing the development of model sequences that probe different parameter regimes. Our experimental approach to studying SASI and convection follows similar works (Foglizzo et al. 2006; Ohnishi et al. 2006; Scheck et al. 2008; Fernández & Thompson 2009a; Burrows et al. 2012), to which we relate our findings. To connect with more realistic models, we also test the generality of our analysis results on the simulations of Müller et al. (2012).

The structure of the paper is the following. Section 2 describes the numerical models employed and introduces the Spherical Fourier-Bessel decomposition. Section 3 presents results, separated by exploding and quasi-steady state behavior. A summary and discussion follows in Section 4. Appendix A addresses the stability of the $\ell = 0$ mode in the parametric setup, and Appendix B provides details about the spherical basis functions for the cases of Dirichlet and Neumann boundary conditions.

2   METHODS

2.1   Parametric Hydrodynamic Simulations

2.1.1   Numerical Setup

The parametric, two-dimensional stalled supernova shock simulations employed for the majority of the analysis follow the setup of Fernández & Thompson (2009a,b). These models have been calibrated to the global linear stability analysis of Foglizzo et al. (2007). The linear analysis has been extended to include the effects of parameterized nuclear dissociation and lightbulb neutrino heating (Fernández & Thompson 2009a).

In our time-dependent models, the equations of mass, momentum, and energy conservation are solved in spherical polar coordinates (r, θ), subject to the gravity from a point mass M at the origin and parameterized neutrino heating and cooling:

$$\frac{\partial \rho}{\partial t} + \nabla \cdot (\rho \mathbf{v}) \;=\; 0 \tag{1}$$

$$\frac{\partial \mathbf{v}}{\partial t} + (\mathbf{v} \cdot \nabla)\mathbf{v} \;=\; -\frac{1}{\rho}\nabla p - \frac{GM}{r^2}\hat{r} \tag{2}$$

$$\frac{\mathrm{d}e_{\mathrm{int}}}{\mathrm{d}t} - \frac{1}{\rho}\frac{\mathrm{d}p}{\mathrm{d}t} \;=\; Q_\nu. \tag{3}$$

Here ρ, $\mathbf{v}$, p, and e_{int} are the fluid density, velocity, pressure, and specific internal energy, respectively. The equation of state is that of an ideal gas with adiabatic index γ, i.e., $p = (\gamma - 1)\rho e_{\mathrm{int}}$. To connect with previous studies, the net neutrino source term is set to

$$Q_\nu = \left[\frac{B}{r^2} - A p^{3/2} \right] e^{-(s/s_{\min})^2} \Theta(\mathcal{M}_0 - \mathcal{M}), \qquad (4)$$

where s is the fluid entropy, $\mathcal{M}$ the Mach number, and Θ the step function. This functional form models heating as a lightbulb, with B a normalization constant proportional to the neutrino luminosity. The cooling function, first introduced by Blondin & Mezzacappa (2006) and subsequently used by Foglizzo et al. (2007), models electron and positron capture in an optically thin environment ($\propto \rho T^6$) assuming a radiation-dominated gas ($p \propto T^4$). The exponential suppression at a low entropy $s_{\min}$ is introduced to prevent runaway cooling at the base of the flow, and the cutoff at high Mach number $\mathcal{M}_0 = 2$ is used to suppress heating and cooling in the upstream flow (Fernández & Thompson 2009a).

The initial condition consists of a steady-state spherical accretion shock at a radius r_s, below which the fluid settles subsonically onto a protoneutron star of radius r_*. Given a boundary condition at the shock, the normalization of the cooling function A is determined by demanding that the radial velocity vanishes at $r = r_*$. The upstream flow is supersonic and adiabatic, with zero Bernoulli parameter. The Mach number upstream of the shock is set to $\mathcal{M}_1 = 5$ at a radius r_{s0} equal to the shock radius obtained with zero heating ($B = 0$). To connect with previous studies (e.g., Fernández & Thompson 2009a), the adiabatic index is set to $\gamma = 4/3$, even though a more realistic flow would have this index varying within the range $1.4 - 1.6$. A constant specific energy loss by nuclear dissociation ε is allowed at the shock, increasing the compression ratio (Thompson 2000). The solution is uniquely determined by specifying the ratio r_*/r_{s0}, the nuclear dissociation parameter ε, the upstream Mach number $\mathcal{M}_1$, and the heating rate B (see Fernández & Thompson 2009a for a sample of initial density profiles). In all models, we set $r_*/r_{s0} = 0.4$.

Throughout this paper, we adopt the initial shock radius without heating, r_{s0}, the free fall speed at this radius, $v_{\mathrm{ff0}}^2 = 2GM/r_{s0}$, and the upstream density ρ_1 as the basic system of units. Full-scale simulations yield characteristic values $r_{s0} \simeq 150$ km, $M \simeq 1.3 M_\odot$, and $\dot{M} \simeq 0.3 M_\odot\ \mathrm{s}^{-1}$, with a resulting free-fall speed $v_{\mathrm{ff0}} \simeq 5 \times 10^9\ \mathrm{cm\ s}^{-1}$, dynamical time $t_{\mathrm{ff0}} = r_{s0}/v_{\mathrm{ff0}} \simeq 3$ ms, and upstream density $\rho_1 \simeq 10^8\ \mathrm{g\ cm}^{-3}$. Setting the heating term in equation (4) equal to the approximation from Janka (2001) commonly used in 'lightbulb' heating studies (e.g., Murphy & Burrows 2008; Couch 2013b), one obtains a relation between B and the electron neutrino luminosity,

$$B \simeq 0.009\, L_{\nu_e,52}\, T_{\nu,4}^2 \left(\frac{r_{s0}}{150\ \mathrm{km}} \right)^{1/2} \left(\frac{1.3 M_\odot}{M} \right)^{3/2}, \qquad (5)$$

where $L_{\nu_e,52}$ is the electron neutrino luminosity in units of $10^{52}\ \mathrm{erg\ s}^{-1}$, and $T_{\nu,4}$ is the neutrinospheric temperature in units of 4 MeV.

The numerical models are evolved in FLASH3.2 (Dubey et al. 2009), with the modifications introduced in Fernández (2012). The computational domain covers the radial range $r \in [0.4, 7] r_{s0}$, and the full range of polar angles. The radial grid spacing is logarithmic, with 408 cells in radius ($\Delta r/r \simeq 0.7\%$). We use 300 angular cells equispaced in $\cos\theta$, yielding constant volume elements at fixed radius ($\Delta\theta \simeq \Delta r/r$ on the equator). The boundary conditions are

reflecting at the polar axis and at the surface of the neutron star, and set to the upstream solution at the outer radial boundary. Accreted material accumulates in the innermost $\sim$ two cells next to the inner boundary.

2.1.2 Models Evolved and Initial Perturbations

Based on the linear stability analysis of Foglizzo et al. (2006), the transition from SASI- to convection-dominated behavior occurs when the parameter

$$\chi = \int_{r_g}^{rs} \frac{\mathrm{Im}(\omega_{\mathrm{BV}})}{|v_r|}\, \mathrm{d}r, \qquad (6)$$

exceeds a critical value of the order of 3. Here r_g is the gain radius, ω_{BV} is the buoyancy frequency,

$$\omega_{\mathrm{BV}}^2 = \frac{GM}{r^2} \left[\frac{1}{\gamma} \frac{\partial \ln p}{\partial r} - \frac{\partial \ln \rho}{\partial r} \right] \qquad (7)$$

and v_r is the radial velocity. This critical value of χ is the number of e-foldings by which an infinitesimal buoyant perturbation needs to grow to counter advection out of the gain region. Larger heating rates and longer advection times are favorable for the growth of convection, as they increase χ.

A finite-amplitude density perturbation can also overcome the stabilizing effect of advection when $\chi < 3$. The minimum amplitude required for a perturbation to rise buoyantly against the accretion flow is (Thompson 2000; Scheck et al. 2008; Fernández & Thompson 2009a; Dolence et al. 2013; Couch 2013a)

$$\left(\frac{\Delta\rho}{\rho} \right)_{\mathrm{c}} \simeq \frac{C_D\, v_2^2}{2 l_v\, g_s} \qquad (8)$$

where v_2 and g_s are the postshock velocity and gravitational acceleration at the shock, respectively, C_D is the drag coefficient of the perturbation ($\simeq 0.5$ for a sphere), and l_v is the ratio of the volume to the cross-sectional area of the perturbation in the direction of gravity (4/3 times the radius, for a sphere).

We evolve two different sequences of models for which the heating rate B is varied from zero to a value that yields an explosion in 2D, and a third set of models that explores the effect of large-amplitude perturbations on a SASI-dominated background state. All models are summarized in Table 1.

The first sequence (e0) is such that all models are well within the $\chi < 3$ regime, corresponding to a SASI-dominated system. This background flow is obtained by setting the dissociation parameter ε to zero. The flow is initially perturbed everywhere with random cell-to-cell velocity fluctuations, with an amplitude 0.1% of the local radial velocity.

The second sequence (e3) has the dissociation parameter set to 30% of the gravitational energy at the shock position without heating ($r = r_{s0}$). The larger density jump yields smaller postshock velocities (Fernández & Thompson 2009b), increasing the value of χ. Most of the models in this sequence lie in the $\chi > 3$ regime, and are therefore convection-dominated. This combination of parameters is the same as used in one of the sequences of Fernández & Thompson (2009a). The same set of initial perturbations as in the e0 sequence are used.

A third set of models (p0) has large-amplitude initial perturbations applied mostly to the exploding model

Table 1. Models Evolved and Results. Columns show model name, dissociation parameter, heating constant (eq. [4]), initial convection parameter (eq. [6]), minimum amplitude for convection (eq. [8]) assuming a spherical bubble with $l_v = 2(r_s - r_g)/3$, initial gain and shock radius, type and amplitude of initial perturbation (§2.1.2), advection time and convection parameter of time-averaged flow (eq. [24]), ratio of time-averaged kinetic energy to time-averaged mass in the gain region (non-exploding), and time $t_{\rm exp}$ at which the shock hits the outer radial boundary (exploding). The unit system is defined in §2.1.1.

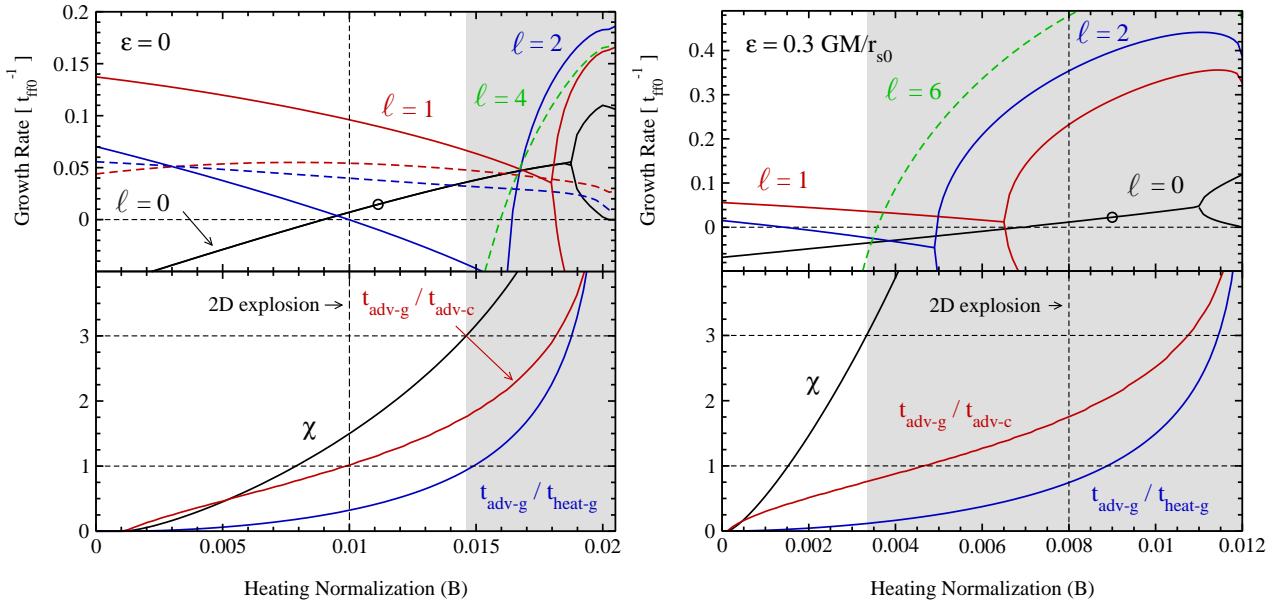| Model	ε $(v_{\rm ff0}^2/2)$	B $(r_{\rm s0}v_{\rm ff0}^3)$	χ_0	$(\Delta\rho/\rho)_{\rm c}$	r_g	r_s $(r_{\rm s0})$	Pert.	Ampl.	$\bar{t}_{\rm adv}$ $(t_{\rm ff0})$	$\bar{\chi}$	$E_{\rm kin,g}/M_{\rm g}$ $(10^{-2}\,v_{\rm ff0}^2)$	$t_{\rm exp}$ $(t_{\rm ff0})$
e0B00	0	0	0	...	...	1	rand. $\delta\mathbf{v}/v_r$	10^{-3}	8.9	0	...	...
e0B02		0.002	0.06	0.14	0.90	1.04			9.5	0.69	3.7	...
e0B04		0.004	0.3	0.07	0.78	1.09			10.2	0.64	2.9	...
e0B06		0.006	0.6	0.05	0.72	1.14			11.3	0.81	2.7	...
e0B08		0.008	1.0	0.05	0.69	1.20			13.1	1.06	2.7	...
e0B10		0.010	1.5	0.04	0.67	1.28			...	...	...	336
p0B08L1	0	0.008	1.0	0.05	0.69	1.20	$\ell = 1$ shell	0.1	12.5	1.2	2.3	...
p0B10L1		0.010	1.5	0.04	0.67	1.28			...	...	...	218
p0B10L2							$\ell = 2$ shell		...	...	...	376
p0B10R1							rand. $\delta\rho/\rho$	0.1	...	...	...	127
p0B10R3								0.3	...	...	...	241
p0B10G4							$\ell = 4$ gain	0.5	...	...	...	246
p0B10G5							$\ell = 5$ gain		...	...	...	122
e3B00	0.3	0	0	...	...	1	rand. $\delta\mathbf{v}/v_r$	10^{-3}	19.8	0	...	...
e3B02		0.002	1.5	0.021	0.66	1.06			22.5	0.89	0.9	...
e3B04		0.004	3.9	0.016	0.60	1.13			25.5	1.33	1.9	...
e3B06		0.006	7.1	0.013	0.58	1.23			34.8	2.11	2.6	...
e3B08		0.008	8.0	0.010	0.57	1.25			...	...	...	223

Figure 1. Linear stability properties of initial models, as a function of heating rate B (eq. [4]-[5]). Shown are SASI- and convection-dominated sequences (left and right, respectively). *Top:* growth rates for $\ell = 0, 1, 2$ modes in black, red and blue, respectively, with solid and dashed lines for fundamental mode and first overtone, respectively. *Bottom:* dimensionless parameters of the system evaluated in the steady-state solution: convection parameter χ (eq. [6], black), ratio of advection times in the gain and cooling regions (red), and ratio of advection to heating times in the gain region (blue). The shaded area shows the region of parameter space where convection is expected to overcome advection ($\chi > 3$, Foglizzo et al. 2006), open circles signal the onset of $1D$ explosion (Appendix A) and vertical dashed lines the point of $2D$ explosion with the employed resolution (§2.1.1). Green dashed lines show the modes $\ell_{\rm crit}$ from equation (9).

of the e0 sequence. We explore the effect of random cell-to-cell density perturbations in the entire computational domain with an amplitude of 10% and 30%, overdense shells in the upstream flow that trigger specific SASI modes (see Fernández & Thompson 2009b for details), and density perturbations in the gain region which are radially-constant

from r_g to r_s, but with an angular dependence set by a Legendre polynomial. The latter are aimed at exciting convection by large-scale perturbations. The amplitude is chosen to be 50%.

Note that we focus on exploding models that are marginally above the heating rate for explosion, where non-

radial instabilities are expected to have the maximum effect. Further increase of the heating rate yields explosions that develop earlier, eventually approaching the spherically-symmetric runaway condition (e.g., Appendix A).

2.1.3   Linear Stability Properties

The linear stability properties of the two sets of background flow configurations (e0 and e3) are shown in Figure 1. The growth rates of the fundamental $\ell = 1$, and $\ell = 2$ modes as a function of heating rate are monotonically decreasing as long as $\chi < 3$. Above $\chi > 3$, modes transition into a non-oscillatory (convective) state with two branches, in line with the results of Yamasaki & Yamada (2007). The mode $\ell_{\rm crit}$ that bifurcates at the lowest heating rate ($\chi \simeq 3$) is approximately that for which $2\ell_{\rm crit}$ eddies of size $(r_s - r_g)$ fit into a transverse wavelength (Foglizzo et al. 2006)

$$\lambda_{\perp,\rm crit} \equiv \frac{\pi(r_s + r_g)}{\sqrt{\ell_{\rm crit}(\ell_{\rm crit} + 1)}} \sim 2(r_s - r_g). \tag{9}$$

Modes with larger or smaller ℓ bifurcate at higher heating rate.

Figure 1 also shows two important timescale ratios in the stationary solution as a function of heating rates. The first one is the ratio of advection times in the gain and cooling regions, $t_{\rm adv-g}$ and $t_{\rm adv-c}$, respectively. On the basis of numerical simulations with a realistic EOS, Fernández (2012) found that equality between these two timescales at $t = 0$ corresponds approximately to the onset of oscillatory instability. Figure 1 shows that this relation is valid for the $\varepsilon = 0$ sequence, losing accuracy when nuclear dissociation is included.

The *instantaneous* value of the ratio of advection to heating timescales in the gain region has for long been used to quantify proximity to an explosion in numerical simulations (Janka & Keil 1998; Thompson 2000; Thompson et al. 2005). Fernández (2012) found that equality between these two timescales in the *initial condition* – or equivalently, at the time of shock stalling – marks approximately the subsequent onset of non-oscillatory $\ell = 0$ instability in numerical simulations. However, Figure 1 shows that the point where the linear $\ell = 0$ growth rate bifurcates to a non-oscillatory mode lies at a much higher heating rate than the point where $t_{\rm adv-g} = t_{\rm heat-g}$ in both sequences. Nevertheless, it is shown in Appendix A that non-oscillatory instability still sets in at the heating rate for which these timescales are equal in the initial condition, indicating that the expansion is a non-linear effect[1].

2.2   Spherical Fourier-Bessel Spectral Decomposition

To analyze the properties of the flow accounting for its intrinsic spherical geometry, we employ a spherical Fourier-Bessel expansion to perform various spectral decompositions. This set of functions forms an orthogonal basis of two-

---

[1] For the e0 sequence, the e-folding time for the $\ell = 0$ mode is approximately one half of the oscillation period at the heating rate for which $t_{\rm adv-g} = t_{\rm heat-g}$.

or three-dimensional space in spherical coordinates, allowing the expansion of an arbitrary scalar function $f(r, \theta, t)$ in a series of the form

$$f(r, \theta, t) = \sum_{n,\ell} f_{n\ell}(t) g_\ell(k_{n\ell}r) P_\ell(\cos\theta), \tag{10}$$

where $g_\ell(k_{n\ell}r)$ are the radial basis functions, $k_{n\ell}$ is the radial wave number of order n, $P_\ell(\cos\theta)$ are the Legendre polynomials of index ℓ, and $f_{n\ell}(t)$ are (time-dependent) scalar coefficients. Expansions of this form have previously been used in the context of galaxy redshift surveys (e.g., Fisher et al. 1995). Appendix B contains a detailed description of the expansion method, including the straightforward extension to three-dimensional space. In what follows we provide a brief outline, focusing on the quantities needed to analyze the turbulent flow in our 2D models.

The domain considered is the volume enclosed between two concentric spheres of inner and outer radii $r_{\rm in}$ and $r_{\rm out}$, respectively. These spherical surfaces can be any pairwise combination of the neutrinosphere, gain radius, or shock radius, depending on the particular region to be studied. The radial basis functions $g_\ell(k_{n\ell}r)$ are linear combinations of spherical Bessel functions j_ℓ and y_ℓ, with coefficients chosen to satisfy specific boundary conditions at both interfaces (Appendix B).

Imposing these boundary conditions generates a set of discrete radial wave numbers $k_{n\ell}$, in analogy with the modes of a membrane in cylindrical coordinates. In addition to its quantum numbers n and ℓ, these wave numbers depend on the chosen ratio of inner and outer radii $r_{\rm in}/r_{\rm out}$. Appendix B derives the wave numbers, relative coefficients, and normalization of the radial basis functions for the cases of vanishing (Dirichlet) and zero gradient (Neumann) boundary conditions. For low n, ℓ, and $r_{\rm in}/r_{\rm out} \to 1$, these wave numbers approach

$$k_{n\ell} \to \frac{\pi}{(r_{\rm out} - r_{\rm in})}(n + 1), \quad (n = 0, 1, 2, ...) \tag{11}$$

increasing in value for stronger curvature. The normalized basis functions satisfy the orthogonality relation (equations B8 and B17)

$$\int_{r_{\rm in}}^{r_{\rm out}} r^2 \mathrm{d}r \, g_\ell(k_{n\ell}r) g_\ell(k_{m\ell}r) = \delta_{nm}. \tag{12}$$

The coefficients for the spherical Fourier-Bessel expansion in equation (10) are thus

$$f_{n\ell}(t) = \frac{2\ell + 1}{2} \int f(r, \theta, t) g_\ell(k_{n\ell}r) \, P_\ell(\cos\theta) \, r^2 dr \, \sin\theta \mathrm{d}\theta. \tag{13}$$

From Parseval's identity,

$$\int |f|^2 \, \mathrm{d}^2 x = \sum_{n,\ell} \frac{2}{2\ell + 1} \, |f_{n\ell}|^2, \tag{14}$$

one can define a discrete power spectral density in 2D space

$$P_{n\ell} = \frac{2}{2\ell + 1} \, |f_{n\ell}|^2. \tag{15}$$

The coefficients $f_{n\ell}(t)$ can also be Fourier analyzed in time, yielding an individual power spectrum for each (n, ℓ) mode. Using a Discrete Fourier Transform (DFT) in time, the normalization can be taken to be the time-average of the volume

integral of the variable in question (e.g., Press et al. 2006),

$$\frac{1}{N_q}\sum_q \int |f|\, \mathrm{d}^2 x \quad = \quad \frac{1}{N_q^2}\sum_{n\ell q}\frac{2}{2\ell+1}|\widehat{f}_{n\ell q}|^2 \tag{16}$$

$$\equiv \quad \sum_{n\ell q}\mathcal{P}_{n\ell q}, \tag{17}$$

where N_q is the number of time samples, and $\widehat{f}_{n\ell q}$ is the DFT of $f_{n\ell}(t)$ at frequency q.

In practical applications, the series in equation (14) must be truncated at a finite value of the indices. In our analysis we set these maximum indices to be at most half the number of grid points in the corresponding direction, in analogy with the Nyquist limit in cartesian coordinates.

2.3 General Relativistic, Radiation-Hydrodynamic Simulations

We use the set of two-dimensional, general-relativistic, radiation-hyrodynamic simulations of Müller et al. (2012) to test the validity of the general principles inferred from the parametric models. The Müller et al. (2012) models follow the evolution of a star of mass $8.1 M_\odot$ and metallicity $Z = 10^{-4}$ (A. Heger 2013, private communication), and a $27 M_\odot$ star of solar metallicity (Woosley et al. 2002). The code employed is VERTEX-CoCoNuT (Müller et al. 2010), which treats multi-group neutrino transport using the 'ray-by-ray-plus' approach (Rampp & Janka 2002; Bruenn et al. 2006; Buras et al. 2006).

These two successfully exploding models follow very different paths on their way to runaway expansion. The $8.1 M_\odot$ progenitor (model u8.1) becomes dominated by convection shortly after the shock stalls, and remains so until runaway sets in. In contrast, the $27 M_\odot$ model (s27) develops a strong SASI throughout the evolution.

3 RESULTS

3.1 Transition to Explosion

We first concentrate on the differences in the transition to explosion introduced by the initial dominance of the SASI or convection. To this end, we focus the discussion on models that bracket the critical heating rate for explosion (Table 1). We then discuss the effect of different initial perturbations on exploding models.

3.1.1 Interplay of SASI and Convection

The characteristic behavior of models with an early dominance of the SASI is illustrated in Figures 2 and 3. Initially, the $\ell = 1$ shock Legendre coefficient displays sinusoidal oscillations of exponentially growing amplitude. While in models without heating the SASI grows in amplitude until oscillations saturate while keeping its characteristic period (e.g., Fernández & Thompson 2009b), in models with significant heating this period increases when the amplitude becomes large, and eventually the regularity of the oscillation is lost.

This breakdown of the SASI cycle is due to large-scale, long-lived fluid parcels with enhanced entropy emerging in the post-shock region. These structures are seeded during
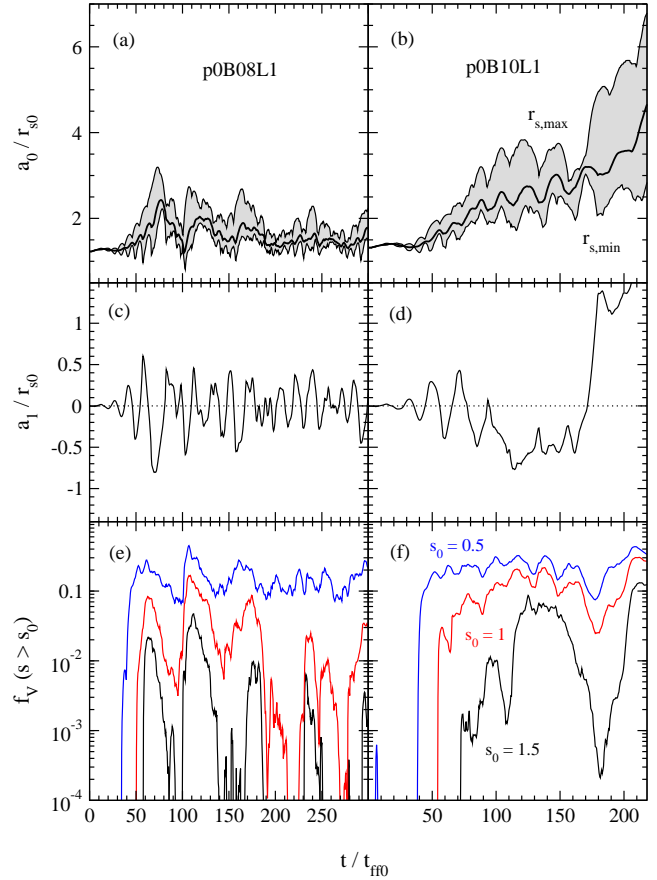

Figure 2. Time-series diagnostics for SASI-dominated models below and above the threshold for explosion (p0B08L1 and p0B10L1, respectively). The $\ell = 1$ SASI mode is excited with an overdense shell. The top panels shows $\ell = 0$ Legendre coefficient (eq. [18]) of the shock surface (thick line), as well as minimum and maximum shock radii (thin lines). Middle panels show $\ell = 1$ shock Legendre coefficient. Bottom panels show the fraction of the post-shock volume with an entropy higher than a given value (eq. [19]). Note that bubble destruction (sudden decreases in f_V for high entropy) precedes large amplitude sloshings of the shock (as indicated by a_1 changing sign). The unit of length is the initial shock radius without heating r_{s0} and the unit of time is the free-fall time at this position (~ 3 ms for a central mass of $1.3 M_\odot$ and $r_{s0} \sim 150$ km, §2.1.1).

shock expansions (Figure 3a; see also Scheck et al. 2008). For small shock displacements, these elongated bubbles are shredded by lateral flows inherent in the SASI, and are advected out of the gain region, allowing the advective-acoustic cycle to proceed as in the case without heating. Above a certain amplitude, however, bubbles are able to resist shredding, and the SASI cycle is interrupted. Accretion proceeds then along narrow downflows that circumvent the bubbles (Figure 3b).

To quantitatively analyze the interplay between sloshing of the post-shock region and large-scale bubbles, we compare in Figure 2 the evolution of the $\ell = 1$ shock Legendre coefficient a_1, where

$$a_\ell(t) = \frac{2\ell+1}{2}\int_0^\pi r_s(\theta,t)P_\ell(\cos\theta)\sin\theta\,\mathrm{d}\theta, \tag{18}$$
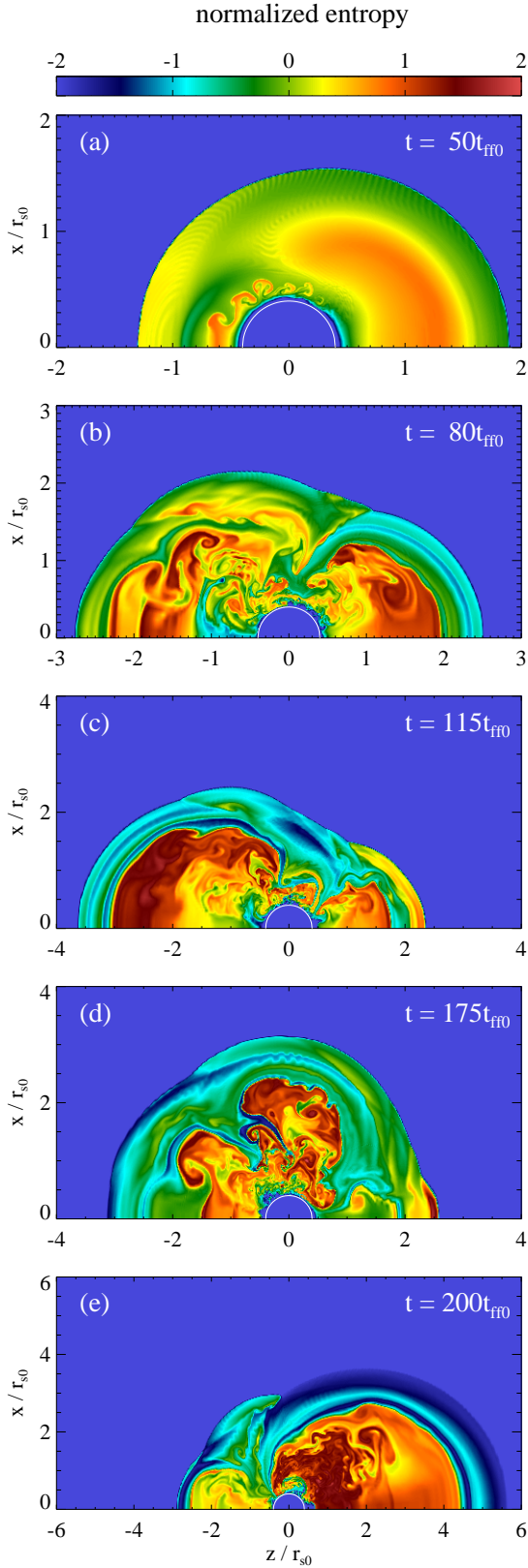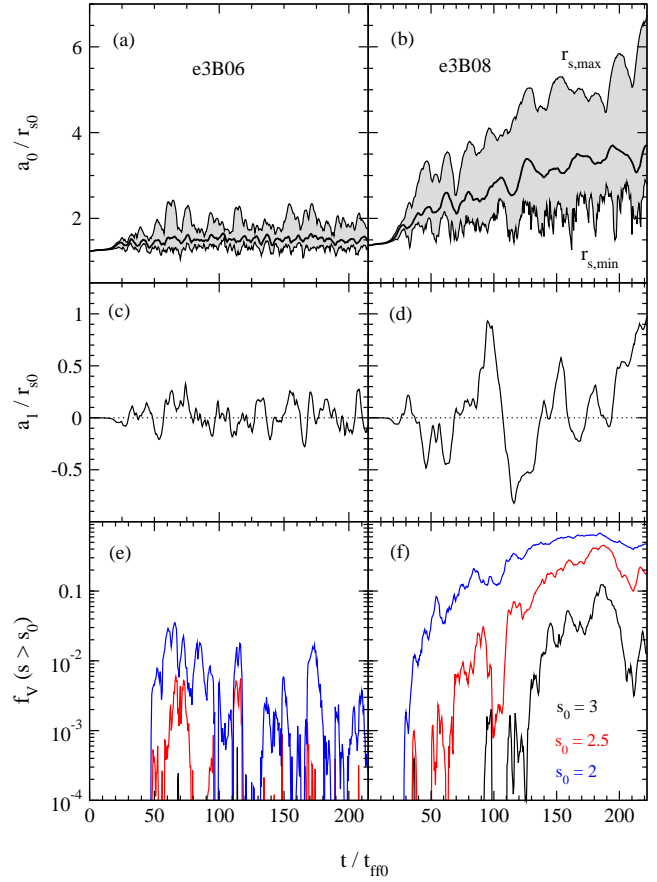
Figure 4. Same as Figure 2, but for convection-dominated models that bracket the threshold for explosion (e3B06 and e3B08). Even though $\ell = 1$ shock oscillations have no clear periodicity, the relation between destruction of high-entropy bubbles and large amplitude shock sloshings is still present. The unit of length is the initial shock radius without heating r_{s0} and the unit of time is the free-fall time at this position (~ 3 ms for a central mass of $1.3 M_\odot$ and $r_{s0} \sim 150$ km, §2.1.1).

Figure 3. Entropy at selected times in the evolution of model p0B10L1, which explodes SASI-dominated. Panels show the seeding of perturbations in one hemisphere and bubble disruption on the other (a), loss of coherence of SASI (b), development of first large bubble (c), partial disruption and displacement of bubble (d), and final expansion (e). Compare with Figure 2.

with the fraction of the post-shock volume with entropy higher than a fiducial value s_0:

$$f_V(s > s_0) = \frac{1}{V} \int_{s_0}^{\infty} \frac{dV}{ds} ds, \tag{19}$$

where the entropy

$$s = \frac{1}{\gamma - 1} \ln \left[\frac{p}{p_s} \left(\frac{\rho_2}{\rho} \right)^{\gamma} \right] \tag{20}$$

is defined so that it vanishes below the shock in the initial model (p_2 and ρ_2 are the initial post-shock pressure and density, respectively; e.g. Foglizzo et al. 2007), and the post-shock volume is defined as

$$V(t) = 2\pi \int_0^{\pi} \int_{r_*}^{r_s(\theta, t)} r^2 dr \sin \theta d\theta. \tag{21}$$

We use volume instead of mass to minimize the influence of low-entropy downflows. The emergence of peaks in $f_V(t)$ for high values of the entropy is related to the loss of periodicity and eventual halting of shock sloshings, while bubble destruction can allow regular periodicity to emerge again (c.f. Figure 2c,e in the range $t \in [200, 250] t_{ff0}$).

Large-scale bubbles that have halted the SASI can nevertheless be broken when low-entropy downflows bend and flow laterally. This process triggers bubble disruption, and results in their shredding or displacement to the opposite hemisphere (Figure 3). Accretion is then able to proceed through the whole hemisphere previously occupied by the bubble, and the shock executes a sloshing (c.f. Figure 2d,f in the range $t \in [150, 200]t_{\mathrm{ff0}}$, also Figure 3d). The shock retractions are related to a decrease in pressure support triggered by an increase in cooling. The buoyancy of high-entropy bubbles blocks the flow of gas to the cooling region, resulting in a lower amount of cooling per SASI cycle and a loss of periodicity in the shock oscillations.

The key difference between exploding and non-exploding models appears to be whether the system can form entropy perturbations of sufficient size and amplitude. Model p0B10L1 displays such an entropy enhancement at time $t \sim 115t_{\mathrm{ff0}}$. This enhancement is perturbed and displaced around time $t \simeq 175t_{\mathrm{ff0}}$, triggering a large sloshing of the shock that transitions into runaway expansion. In contrast, model p0B08L1 fails to develop a long-lived structure with entropy higher than $s > 1.5$. The transition to explosion for a large enough bubble results from the relative importance of buoyancy and drag forces (Thompson 2000).

The characteristic evolution of convection-dominated models is illustrated by Figure 4. Entropy enhancements are initially generated by convection. Bubbles grow and merge into large-scale structures, which cause non-linear shock displacements. In non-exploding models, bubbles have a short lifetime, and hence the shock undergoes sloshings of moderate amplitude over a range of temporal frequencies. Note that the destruction of large bubbles can also lead to shock sloshings, but the persistent generation of entropy fluctuations of smaller scale and amplitude prevent the emergence of SASI oscillations with a well-defined periodicity.

For high enough heating rate, large bubbles are able to survive for many eddy turnover times, leading to explosion in a manner similar to that of SASI-dominated models. The role of high-entropy bubbles in convection-dominated models has been documented previously (Dolence et al. 2013; Couch 2013a).

3.1.2 Effect of Initial Perturbations

The effect of different initial perturbations on the exploding model of the e0 sequence is illustrated in Figure 5. Models with large amplitude random cell-to-cell density perturbations (p0B10R1 and pB10R3) follow the same path as the model where $\ell = 1$ is directly perturbed (p0B10L1, Fig. 2). The model with an $\ell = 2$ perturbation (p0B10L2) undergoes a weak convective phase over a number of advection times, during which $\ell = 0$ grows and $\ell = 2$ saturates at a small amplitude. After a delay of $\sim 100t_{\mathrm{ff0}}$, however, $\ell = 1$ oscillations of the shock emerge, and the model joins the usual SASI-dominated explosion path. The models with large amplitude density perturbations in the gain region with a fixed $\ell = 4$ and 5 dependence (p0B10G4 and p0B10G5) trigger less regular sloshings of the shock, which however still result in the formation of large-scale bubbles. As with the $\ell = 2$ perturbation, an even-ℓ convective perturbation takes longer to couple to an $\ell = 1$ SASI mode.

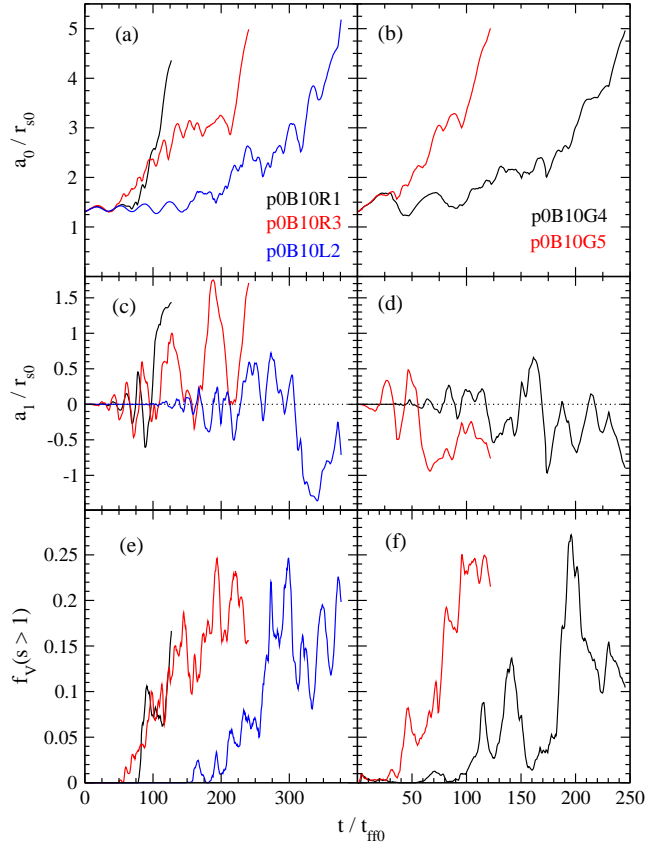The time to explosion appears to be a non-trivial

Figure 5. Time-series diagnostics for exploding models with different initial perturbations (Table 1). Top panels show average shock radius, middle panels show $\ell = 1$ shock Legendre coefficient, and bottom panel shows fraction of the postshock volume with entropy higher than unity. Note the longer time to explosion and late onset of $\ell = 1$ oscillations in models with even ℓ perturbations (p0B10L2 and p0B10G4). The unit of length is the initial shock radius without heating r_{s0} and the unit of time is the free-fall time at this position (~ 3 ms for a central mass of $1.3M_\odot$ and $r_{\mathrm{s0}} \sim 150$ km, §2.1.1).

function of the perturbation form and amplitude. Model p0B10R3 has larger amplitude perturbations, yet it hits the outer boundary 100 dynamical times later than model p0B10R1. Despite the very large amplitude perturbation of model p0B10G4, it explodes later than all models with an odd ℓ perturbation. This strong sensitivity to initial conditions has been documented previously by Scheck et al. (2006).

We emphasize however that we are focusing on models that are barely above the threshold for explosion. Recently, Couch & Ott (2013) have pointed out the importance of pre-collapse perturbations in tilting the balance towards explosion. Such an effect is likewise only going to make a difference if a model is already close to exploding in the absence of perturbations. For instance, models e0B10 and p0B10L1 differ in the type and amplitude of perturbations, leading to explosions that differ by more than 100 dynamical times in onset. In contrast, neither of models e0B08 or p0B08L1 explode, despite the fact that they mirror the exact perturbations as the previous two exploding models (the latter having a 10% density perturbation in the form of a thin shell).
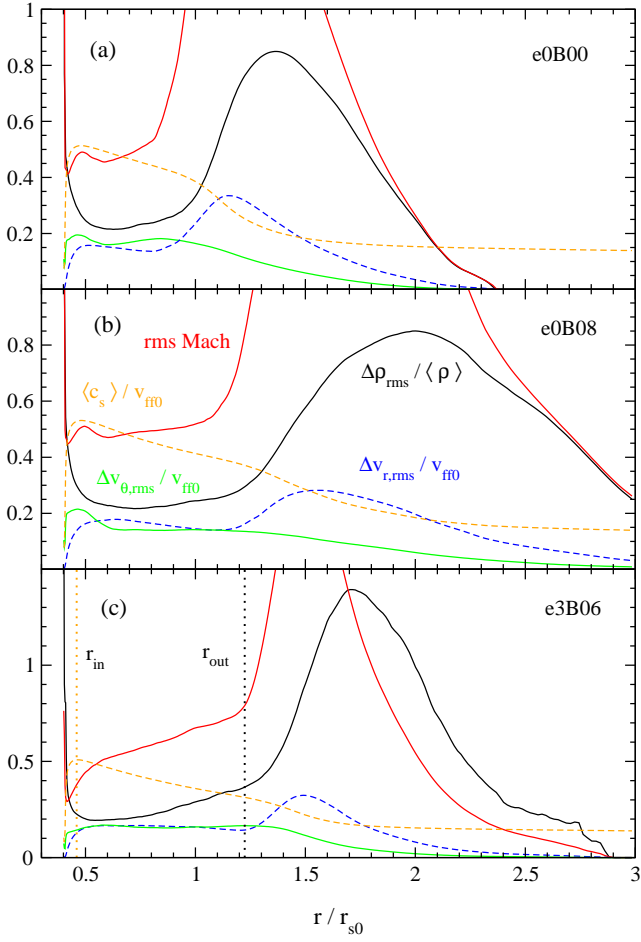
Figure 6. Time- and angle-average profiles of selected quantities for non-exploding models. Top, middle, and bottom panels show models with no heating (e0B00), SASI-dominated close to explosion (e0B08), and convection-dominated close to explosion (e3B06), respectively. Curves correspond to r.m.s. density fluctuation normalized to its mean value at each radius (eqns. [22]-[23], solid black), r.m.s. Mach number (solid red), r.m.s. radial velocity (dashed blue), r.m.s. meridional velocity (solid green), and average sound speed (dashed orange). The vertical dotted lines in panel (c) bracket the radial range where the post-shock flow is subsonic and free from strong stratification effects, with r_{in} and r_{out} corresponding to the peak of the average sound speed, and the average of the minimum shock radius minus its r.m.s. fluctuation (c.f. Fig. 8 of Fernández & Thompson 2009b), respectively.

From our results it is not obvious that a large enough density perturbation suffices to turn a model for which the background state is SASI-dominated into a convectively dominated model. Note however that our models have $\chi \ll 3$. Previous studies have witnessed more sensitivity to the type of initial perturbation when the χ parameter at shock stalling is close to or even transiently exceeds criticality (Scheck et al. 2008; Hanke et al. 2013).

The 'purity' of an excited $\ell = 1$ SASI mode also depends on whether the background flow allows for unstable harmonics. Figure 1 shows that the first $\ell = 1$ overtone is unstable for all the heating rates in the e0 sequence. This may lead to shock oscillations that are not a clean sinusoid, but which should not be mistaken as an imprint of convection.
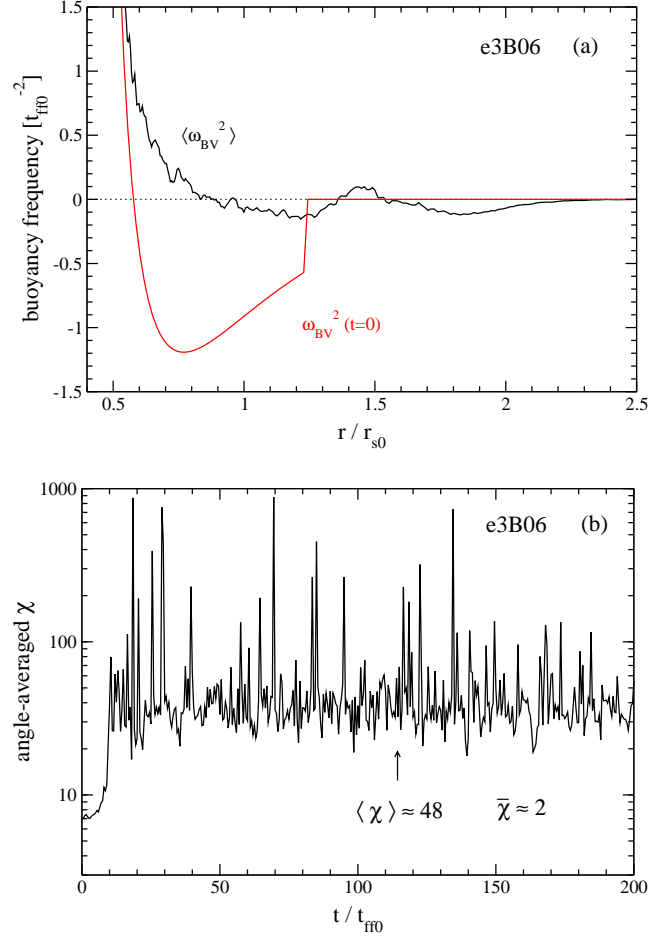

Figure 7. *Top:* Squared buoyancy frequency (eq. [7]) as a function of radius for a convection-dominated model close to explosion (e3B06). Curves show initial (red) and time-angle-averaged values (black). *Bottom:* angle-averaged convection parameter as a function of time for the same model (e3B06). The time average value $\langle \chi \rangle$ is much larger than what is obtained when computing this parameter with quantities from the time-averaged flow, $\bar{\chi}$ (eq. [24]), because χ is a non-linear function.

3.2   Properties of the Quasi-Steady State

We now address the properties of the turbulent flow in the gain region in cases where an explosion is not obtained, focusing on the differences between models where either SASI or convection dominate. We first discuss general properties of the time-averaged flow, and then analyze models using a spherical Fourier-Bessel decomposition in space and a discrete Fourier transform in time.

3.2.1   *Time-Averaged Flow and Convective Stability*

The spatial structure of the quasi-steady-state becomes clear when the flow is averaged in angle and time (e.g., Fernández & Thompson 2009b). Figure 6 shows such a representation for a model without heating (e0B00), as well as SASI- and convection-dominated models close to an explosion (e0B08 and e3B06, respectively). The time- and angle-average of a generic scalar quantity is denoted by

$$\langle A(r) \rangle = \frac{1}{2(t_f - t_i)} \int_{t_i}^{t_f} dt \int_0^\pi A(r, \theta, t) \sin\theta d\theta, \qquad (22)$$

where $[t_i, t_f]$ is the time interval considered for the average, and the corresponding root-mean-square (r.m.s.) fluctuation is defined as

$$\Delta A_{rms} = \left[\langle A^2 \rangle - \langle A \rangle^2 \right]^{1/2}. \qquad (23)$$

All three models share a basic general structure. From the inside out, this structure is composed of a narrow cooling layer adjacent to r_*, a region of sub-sonic turbulence encompassing part of the cooling layer and part of the (time-averaged) gain region, an extended zone of shock oscillation, and the unperturbed upstream flow.

The most notorious difference among these models lies in the properties of the shock oscillation zone and in the flow around the cooling layer. Models where the SASI dominates have a wider shock oscillation zone than the model where convection is dominant. This can be seen by comparing the minimum and maximum shock radii of the non-exploding models in Figures 2 and 4. Also, in models where the SASI is prominent there is a bump in the r.m.s lateral velocity in the cooling layer, indicating strong shear. This bump is absent in the convection-dominated model.

In contrast, the subsonically turbulent region has very similar properties in the three different models shown in Figure 6, with only slight changes in the radial slopes. Characteristic values are $\Delta\rho_{rms}/\langle\rho\rangle \sim 0.25$, r.m.s. Mach number ~ 0.5, and $\Delta v_{r,rms} \simeq \Delta v_{\theta,rms} \sim 0.15 v_{ff0}$. This similarity in time-averaged properties suggests that flows are not very different from each other.

By analogy with convective systems in steady-state (e.g., nuclear burning stars), one can investigate whether the time-averaged system adjusts itself to a state of marginal convective stability. In hydrostatic systems, convection acts to erase destabilizing gradients, whereas the presence of advection in core-collapse supernova flows generates a non-zero entropy gradient in steady-state (Murphy & Meakin 2011). One can nevertheless ask whether the relevant critical parameter for convection is restored to stability in the nonlinear regime.

Figure 7a shows the initial and time-averaged squared buoyancy frequency (eq. [7]) for model e3B06, which is convection dominated. This model has an initial value of $\chi \simeq 7$ (Table 1). The time-averaged flow is such that the degree of convective instability (negative ω_{BV}^2) is significantly weaker than that in the initial state. The implications for convective stability become clear when the χ parameter (eq. [6]) is computed for the time-average flow. One way of doing this is simply averaging χ in time and angle, $\langle\chi\rangle$. However, because this is a non-linear function of the flow variables, the resulting value will not only capture the properties of the mean flow, but it will also include the contribution of turbulent correlations in the pressure, density, and velocity. One can nevertheless still define a convection parameter based on the properties of the mean flow

$$\bar{\chi} = \int \frac{\text{Im}\left(\langle\omega_{BV}^2\rangle^{1/2}\right)}{\langle v_r \rangle} dr, \qquad (24)$$

where the integral extends over regions where $\omega_{BV}^2 < 0$.

The difference between these two ways of computing χ is illustrated in Figure 7b. Shown is the instantaneous

angle-averaged value of χ, together with its time average $\langle\chi\rangle$ as well as the convection parameter computed using the mean flow, $\bar{\chi}$ (eq. [24]). The instantaneous angle-averaged value of χ achieves very large values as soon as the shock displacement becomes non-linear, similar to the results of Burrows et al. (2012), with a time-averaged value $\langle\chi\rangle \sim 50$. The convection parameter from the mean flow is much smaller, however, yielding $\bar{\chi} \simeq 2$. This small number arises from the small magnitude of the time-average of the squared buoyancy frequency shown in Figure 7a.

Values of $\bar{\chi}$ for all non-exploding models are shown in Table 1. All convection-dominated models satisfy $\bar{\chi} < 3$, which indicates that in quasi-steady-state they adjust to a state of convective sub-criticality (the equivalent of 'flat' entropy gradients in hydrostatic systems). The SASI-dominated models maintain $\chi_0 \lesssim \bar{\chi} < 3$, where χ_0 is the value of χ in the initial condition. This *increase* in the time-averaged value of the convection parameter can arise from the increase in the size of the gain region caused by SASI activity, and from the presence of localized entropy gradients induced by the SASI, which trigger secondary convection (e.g., Figure 3a).

It is worth emphasizing that the driving agent matters in characterizing convective motions: secondary convection is qualitatively different from neurino-driven convection in that in the former there are both preferred spatial and temporal scales (entropy perturbations induced by the SASI, and advection time, respectively).

Another aspect of the explosion mechanism that can be probed with the time-averaged flow is the dependence of the turbulent kinetic energy in the gain region on neutrino heating. Hanke et al. (2012) found that a good indicator of the proximity of an explosion is the growth of the turbulent kinetic energy on the largest spatial scales. Since the mass in the gain region also increases due to the larger average shock radius, it is worth clarifying the origin of the increase in the kinetic energy. Table 1 shows the ratio of the total time-averaged turbulent kinetic energy in the gain region to the time-averaged mass in the gain region for non-exploding models. SASI-dominated models are such that this ratio is nearly constant, decreasing slightly when an explosion is closer. Thus larger kinetic energy is due solely to the increase in the mass of the gain region. In contrast, convection-dominated models grow both the specific kinetic energy and the mass in the gain region as an explosion is closer.

3.2.2 Properties of Turbulence in the Subsonic Region

We now use the spherical Fourier-Bessel expansion to analyze the properties of the turbulence in the subsonic region of the time-averaged flow. Operationally, we define the radial limits of this region (r_{in} and r_{out}, §2.2) to be the peak of the time-averaged sound speed, $\langle c_s \rangle$, and the time-average of the minimum shock radius minus its r.m.s. fluctuation, $r_{out} = \langle r_{s,min} \rangle - \Delta r_{s,min,rms}$, respectively. This definition differs from that of Murphy & Meakin (2011) in that we restrict ourselves to radii below the minimum shock position to avoid supersonic flow.

To connect with previous studies, we use the meridional velocity v_θ as a proxy for the turbulent flow. We do not multiply this velocity by $\sqrt{\rho}$, however, because the den-
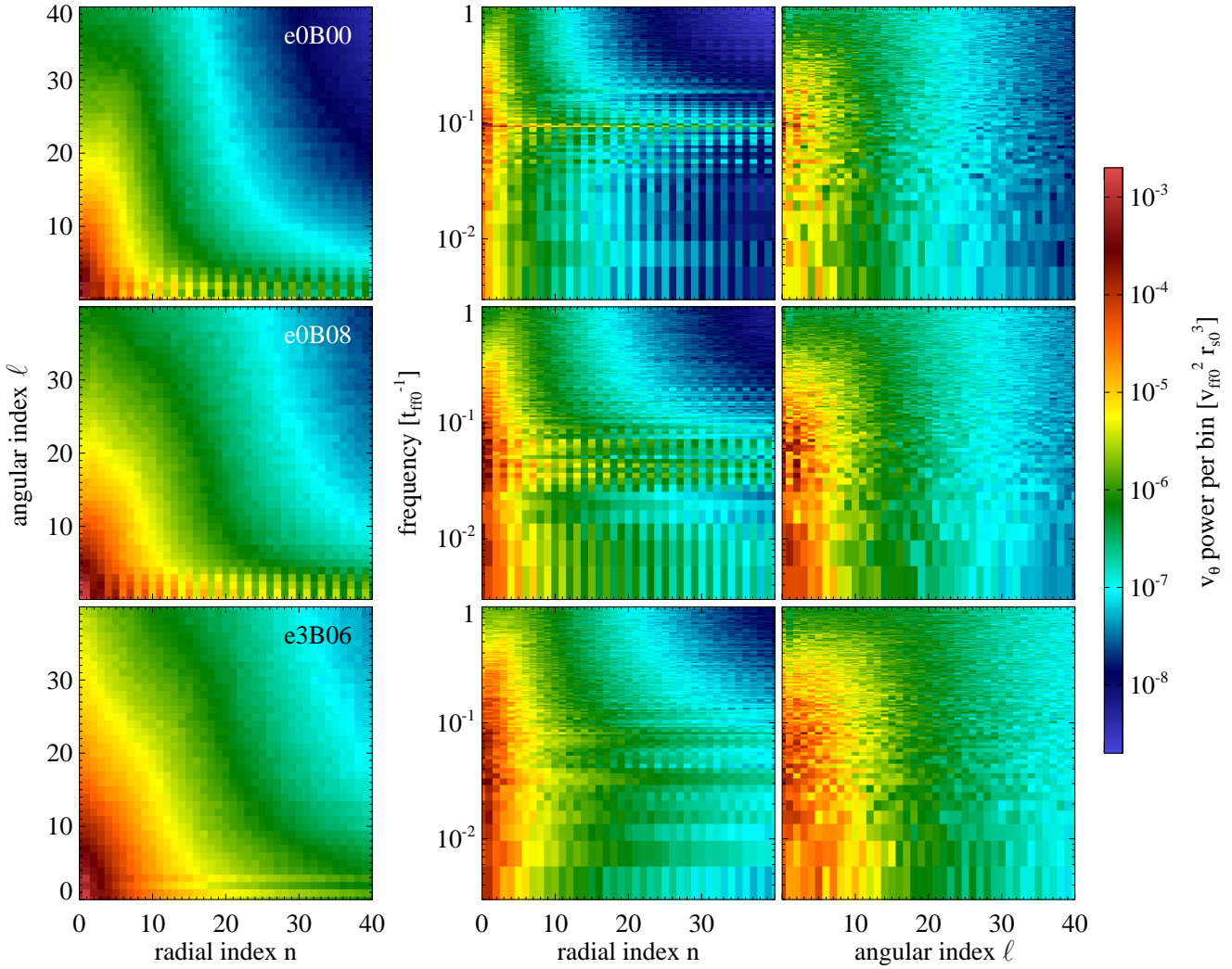
Figure 8. Two-dimensional spherical Fourier-Bessel power spectra, obtained by contracting the three-dimensional space-time power $\mathcal{P}_{n\ell q}$ (eq. [17]) along one dimension, for a model with no neutrino heating (e0B00, top row), a SASI-dominated model close to explosion (e0B08, middle row), and a convection-dominated model close to explosion (e3B06, bottom row). Shown are frequency-summed spatial spectra (left column), ℓ-summed time-n spectra (middle column), and n-summed time-ℓ spectra (right column). Models with a strong SASI display an even-odd pattern in the radial direction at low ℓ, and enhanced power near the advection frequency $\sim 0.1 t_{\mathrm{ff0}}^{-1}$.

sity stratification over the extended radial range considered would affect the spectral slopes (Endeve et al. 2012). Thus, the sum of the total power (eq. [17]) does not approach the total kinetic energy in the subsonic region, but instead it is a measure of the kinetic energy per unit mass.

Figure 8 shows 2D projections of the 3D space-time spectrum $\mathcal{P}_{n\ell q}$ (eq. [17]), for pure SASI, SASI-dominated, and convection-dominated models (c.f. Figure 6). Power is maximal at low angular and radial scales, as expected from the inverse turbulent cascade in 2D (e.g., Davidson 2004). Models where the SASI is prominent display two characteristic features: (1) an even-odd pattern in the radial spectrum for $\ell = 0 - 5$, indicating the presence of discrete modes, and (2) enhanced power around the frequency corresponding to the advection time of the mean flow, $\bar{f}_{\mathrm{adv}} \sim 0.1 t_{\mathrm{ff0}}^{-1}$. The dominance of convection manifests as a broadening of the smoother component of the spatial spectrum to larger n and ℓ, a near disappearance of the even-odd pattern,

and the emergence of power at temporal frequencies below and above $\bar{f}_{\mathrm{adv}}$. This behavior of SASI- and convection-dominated models in the frequency-domain is consistent with the results of Müller et al. (2012) and Burrows et al. (2012).

Figure 9 shows the results of contracting the $\mathcal{P}_{n\ell q}$ array along two dimensions, yielding one dimensional spectra, for models that do not explode. In SASI-dominated models, the normalized power as a function of n shows a characteristic sawtooth shape, which is smoothed to clarify the slope (an example of an non-smoothed spectrum is shown by the gray curve in Figure 9a).

Increasing the heating rate leads to minor changes in the (normalized) radial spectrum in SASI-dominated models. The onset of convection, on the other hand, leads to a shift of power from $n \leqslant 2$ to $n \geqslant 3$. The spectral slope at large n is approximately n^{-2}. This slope could be attributed to Rayleigh-Taylor turbulence, for which the ve-
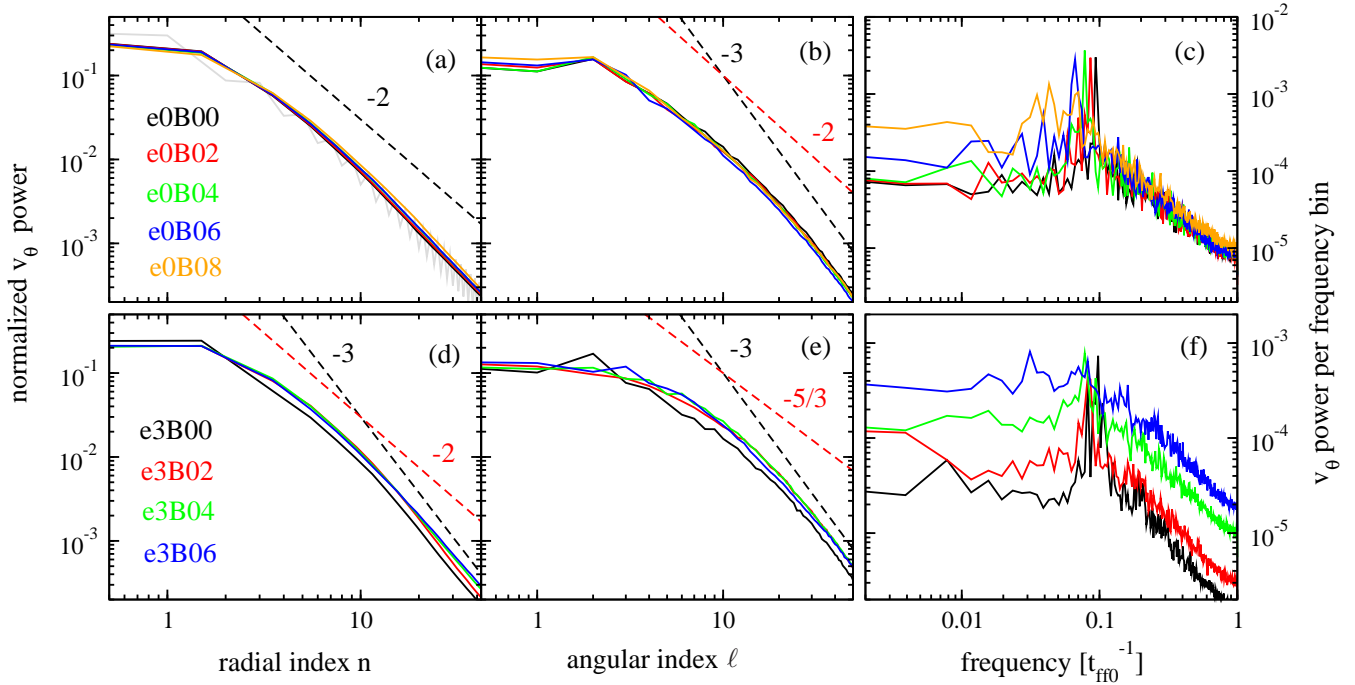
Figure 9. One dimensional spectra for non-exploding models (Table 1), obtained by contracting $\mathcal{P}_{n\ell q}$ (eq. [17]) along two dimensions. The top row shows models in the SASI-dominated sequence (e0) and the bottom row contains convection-dominated models (e3), as labeled. Left, middle, and right columns display radial, angular, and temporal spectra, respectively. The radial spectrum is smoothed by averaging contiguous values; for reference, the unsmoothed spectrum for model e0B00 is shown by the gray curve in panel (a). Dashed lines show reference spectral slopes, labeled by the corresponding exponent.

locity fluctuations satisfy $\delta v \propto \lambda^{1/2}$, with λ the wavelength of the perturbation (e.g., Niemeyer & Woosley 1997; Ciaraldi-Schoolmann et al. 2009). Note however that the wave numbers of the radial basis functions of different ℓ are not harmonic with each other (Fig. B1), hence one cannot straightforwardly map radial wavelength into index n. Nevertheless, the spacing between wave numbers becomes nearly constant at large n, with only a linear shift with ℓ, motivating the use of n as a differential measure of the turbulent cascade.

The angular spectrum in SASI-dominated models shows a peak at $\ell = 2$, and a slope at large ℓ indicative of a direct vorticity cascade (Kraichnan 1967). Similar to the radial spectrum, the onset of convection results in the shift of power from $\ell \leqslant 2$ towards $\ell = 5 - 10$. The resulting spectral shape has a form similar to that found by Hanke et al. (2012), Couch (2013a), and Dolence et al. (2013), who radially averaged the kinetic energy over a thin slice. This shape consists of a shallow curved shape at low ℓ, transitioning to $\sim \ell^{-3}$ slope at large ℓ.

The temporal spectrum of the sequence of convection-dominated models is consistent with the results of Burrows et al. (2012). At very low heating rates, a prominent peak exists at the advection frequency $\bar{f}_{\mathrm{adv}}$, indicating the presence of the SASI. As the heating rate is increased, power increases at frequencies below and above the advection peak. At heating rates close to an explosion, this low-frequency power is comparable or higher than that at $\bar{f}_{\mathrm{adv}}$.

In contrast, the SASI-dominated sequence has a dominant peak at the advection frequency for all models. This peak moves to lower frequencies as heating is increased, be-

cause the advection time increases given the larger average shock radius (Table 1). Also, the peak becomes broader as a likely result of secondary convection being triggered by the SASI. Power at the lowest frequencies still increases with heating rate, but it remains below that in the advection peak by at least a factor of two (in contrast, neutrino-driven convection yields a nearly flat spectrum). Note also that the power at frequencies higher than the advection peak in model e0B08 (SASI-dominated model with the highest heating) is within a factor of two of the convection-dominated model with the highest heating (e3B06).

From Figure 6 one can infer the turnover time of large eddies to be $t_{\mathrm{eddy}} \sim 2\pi r / \Delta v_{\theta,\mathrm{rms}} \sim 30 t_{\mathrm{ff0}}$, yielding a frequency $f_{\mathrm{eddy}} \sim 0.03 t_{\mathrm{ff0}}^{-1}$. Thus, the increase in power at frequencies below the advection time appears to be associated with the evolution of large bubbles in the gain region.

3.3 Application to Full-Scale Core-Collapse Models

Here we analyze the models of Müller et al. (2012) with the same methods used in our parametric models, identifying similarities and differences.

Figure 10 shows the evolution of the $\ell = 0$ and $\ell = 1$ coefficients for models u8.1 and s27, together with the fraction of the volume with entropy higher than fiducial values $s_0 = \{10, 15, 18, 21, 25\}$ k_{B} per baryon. The f_V diagnostic behaves similarly to exploding parametric models p0B10L1 and e3B08 (Figs. 2 and 4). After a large enough fraction of the postshock volume is occupied by high entropy material, the regular periodicity of shock oscillations in model s27 is
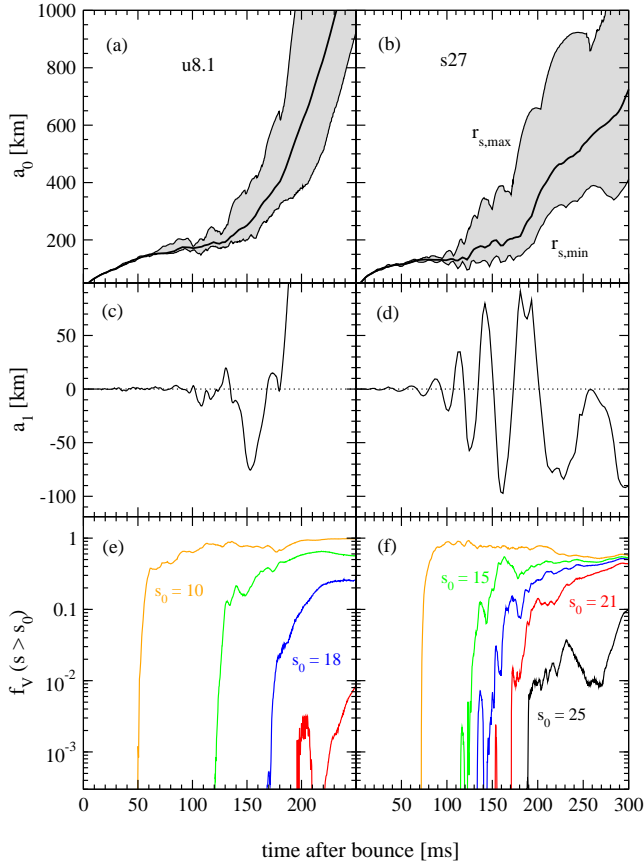
Figure 10. Same as Figure 2, but for models u8.1 and s27 of Müller et al. (2012). The fiducial entropies s_0 are in units of $k_{\rm B}$ per baryon.
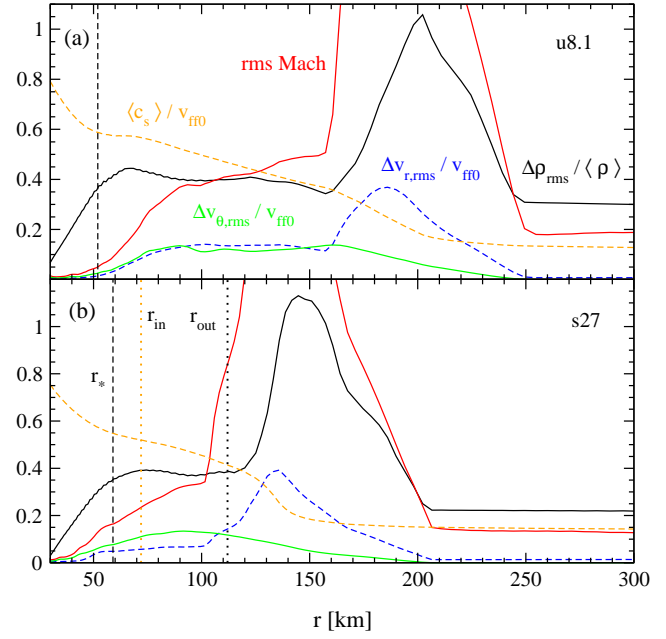

Figure 11. Time- and angle-averaged profiles of selected quantities for models u8.1 and s27 of Müller et al. (2012) (compare with Fig. 6). The free-fall velocity normalization is computed in Newtonian gravity, for gravitational masses $\{1.2, 1.35\}M_\odot$ and initial shock radii $\{150, 130\}$ km for models $\{$u8.1,s27$\}$, respectively. The vertical dashed lines correspond to the time- and angle-averaged radius for which $\rho = 10^{11}$ g cm^{-3}, which we associate with r_*. The vertical dotted lines bracket the radial extent of the region used for spectral analysis (see text for details).

modified ($t \simeq 150$ ms). Shock sloshings in this late stage are preceded by partial disruption of bubbles. One notable difference with model p0B10L1 is the emergence of secondary shocks in model s27, which prevent complete disruption of high-entropy bubbles. Runaway expansion in model s27 is preceded by accretion of the Si/O composition interface. Another important difference between both Müller et al. (2012) models and the exploding parametric models is the level of $\ell = 0$ oscillations, which is much larger in the exploding gamma-law simulations[2].

Models u8.1 and s27 both undergo a quasi-stationary phase that precedes runaway expansion. We have analyzed the properties of the time-averaged flow over the interval $[80, 130]$ ms and $[70, 120]$ ms in models u8.1 and s27, respectively. During these intervals, both the average shock radius and the average neutrinospheric radius r_* (defined as the isodensity surface $\rho = 10^{11}$ g cm^{-3}) change by less than 20%. Figure 11 shows the resulting profiles of time-averaged quantities, in analogy with Figure 6. Above the neutrinosphere, all quantities behave in the same qualitative way as the parametric models. At densities $\rho = 10^{11}$ g cm^{-3} and higher, clear differences are introduced by the existence of a pro-

toneutron star, however. In particular, the density and velocity fluctuations decrease significantly inside r_*, whereas Figure 6 shows a strong increase in the density perturbation near r_* for parametric models due to the accumulation of mass given the reflecting boundary condition, and a bump in the lateral velocity due to shear in SASI-dominated cases. Nonetheless, the very similar behavior of the system outside r_* shows that a reflecting boundary condition is not a bad approximation.

We have also computed the convection parameter using the time-averaged flow (eq. [24]). The buoyancy frequency is computed following Müller et al. (2013) but ignoring relativistic corrections[3]. Model u8.1 has $\bar{\chi} \simeq 0.7$, consistent with the hypothesis that convection-dominated flow adjusts itself to sub-criticality. This parameter is even smaller ($\bar{\chi} \simeq 0.4$) in model s27.

Figure 12 shows one-dimensional spectra of the subsonic region in models u8.1 and s27. The limits of the region are defined to be the saddle point in the time- and angle-averaged sound speed on the inside, and the time-average of the minimum shock radius minus its rms fluctuation on the outside (both radii are shown in Figure 11 for s27). The radial spectrum of the Müller et al. (2012) models has relatively less power at long wavelengths than the parametric models. At short wavelengths, however, the spectral slope is

---

[2] The difference in shock expansion rate once runaway starts is due to the absence of alpha particle recombination in the parametric models (Fernández & Thompson 2009a); this is independent of the level of $\ell = 0$ oscillations.

[3] The leading order corrections to the buoyancy frequency and sound speed scale like $(c_s/c)^2$ (Müller et al. 2013), which is only a few percent in the gain region.
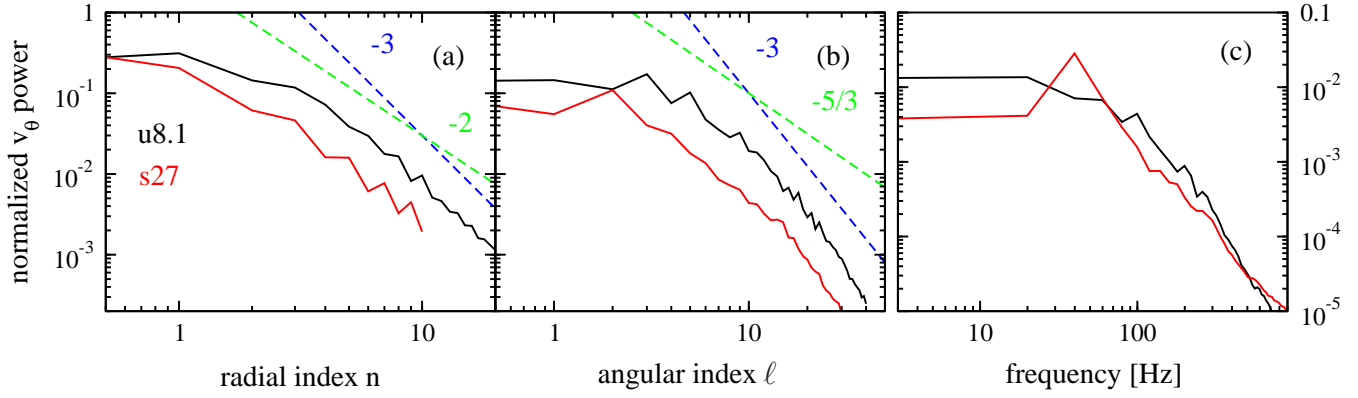
Figure 12. Same as Figure 9, but for models u8.1 and s27 of Müller et al. (2012). The temporal spectrum is normalized so that the frequency integral is unity.

similar, and the sawtooth pattern of SASI-dominated models is also present in model s27 (the spectrum extends to $n = 10$ due to the compactness of the subsonic region relative to the grid spacing). The angular spectrum of model s27 shows the same peak at $\ell = 2$ as the SASI-dominated parametric models. Model u8.1 shows a similar curved shape as convection-dominated models, though with some excess at $\ell = 3$ and $\ell = 5$. Finally, the temporal spectrum shows clearly the distinction between convection-dominance manifesting more power at low frequencies (u8.1), and SASI-dominance generating a clear peak at the advection time (s27). This temporal frequency behavior was already noted by Müller et al. (2012).

In summary, the general results from parametric models regarding SASI- and convection-dominated flow persist in sophisticated, full-scale core-collapse simulations. The use of nuclear dissociation in parametric models as the control parameter for switching between SASI- and convection-dominance does not prevent qualitative agreement with full-scale models, even though the latter always have dissociation present. This is because the behavior of the flow depends chiefly on the *relative timescales* of the system (c.f. §2.1.3).

4   SUMMARY AND DISCUSSION

We have analyzed the transition to explosion in SASI- and convection-dominated core-collapse supernova explosions using parametric, two-dimensional, time-dependent hydrodynamic simulations. These models are such that the linear stability properties are well understood, allowing the exploration of well-differentiated regions of parameter space (Figure 1, Table 1). We have also introduced a spherical Fourier-Bessel decomposition to characterize the properties of turbulence in the sub-sonic region of the flow, to extract signatures of the interplay of SASI and convection. Our main findings are as follows:

1. – The behavior of SASI-dominated models is characterized by the interplay of shock sloshings and the formation of large-scale, high-entropy structures. These bubbles are seeded by the SASI during shock expansions. Regular sloshing of the shock requires that these bubbles have a short lifetime and/or small entropy enhancements. Regular

destruction of high-entropy structures by lateral flows is characteristic of non-exploding models (Figure 2).

2. – Models that explode with SASI dominance are able to form large-scale, high-entropy bubbles that survive for a time longer than a characteristic shock oscillation cycle (Figure 2). Neutrino heating and the inverse turbulent cascade in 2D ensure that these bubbles continue to grow if left undisturbed. Explosion results from the buoyancy of the bubble overcoming the drag force of the upstream flow (Thompson 2000).

3. – Convection-dominated models generate similar large-scale entropy structures by consolidating smaller-scale bubbles arising from buoyant activity. Sloshing of the shock occurs whenever large bubbles are destroyed or displaced, just as in SASI-dominated models, but without a dominant periodicity. The transition to explosion also involves the formation and growth of a sufficiently large bubble (Figure 4), as has been documented previously (Dolence et al. 2013; Couch 2013a).

4. – Initial perturbations with a large amplitude do not alter the qualitative way in which SASI-dominated models explode in two dimensions. The difference in explosion time can be significant, however, and the time to runaway is not a monotonic function of the perturbation amplitude (Figure 5).

5. – The time-averaged flow in convection-dominated, non-exploding models adjusts itself to a state in which the convection parameter computed from the mean flow (eq. [24]) lies below the critical value for convective instability (Table 1). This phenomenon is obscured when an average value of χ is computed from the instantaneous flow (Figure 7).

6. – The spherical Fourier-Bessel power in the subsonic, weakly-stratified region is dominated by the largest spatial scales (Figure 8). The SASI manifests itself as a characteristic even-odd pattern in the radial direction, and enhanced power at temporal frequencies corresponding to the advection time. Convection generates a smoother component, with power concentrated primarily below the

advection frequency. This behavior of the frequency domain is consistent with the results of Burrows et al. (2012) and Müller et al. (2012).

7. – The slope of the angular spectrum is consistent with an inverse turbulent cascade at large ℓ. Convection-dominated models yield angular spectra that resemble those of Hanke et al. (2012), Couch (2013a), and Dolence et al. (2013), while SASI-dominated models show a peak at $\ell = 2$. The radial spectrum shows a scaling n^{-2} at large n, which could be associated with Rayleigh-Taylor turbulence (e.g., Ciaraldi-Schoolmann et al. 2009).

8. – The general results obtained with the parametric models persist when the analysis is repeated on the general relativistic, radiation-hydrodynamic simulations of Müller et al. (2012). In particular, the behavior of the entropy when approaching explosion, and the value of the convection parameter and spectral slopes of the time-averaged flow are in good agreement with the corresponding parametric models.

9. – The equality between advection and heating times in the gain region at $t = 0$ is a good indicator of the onset of non-oscillatory instability in one-dimensional numerical simulations of parametric models (Appendix A), in agreement with the numerical results of Fernández (2012). The fact that this equality occurs for heating rates such that the linear eigenmodes are still oscillatory (Figure 1), however, means that the onset of purely growing expansion is a non-linear effect (growth time shorter than the oscillation period). Initial equality between the advection time in the gain and cooling layers is a good indicator of $\ell = 0$ instability in some regions of the space of parametric models, but not in others, particularly when nuclear dissociation is included (Figure 1). When the recombination energy from alpha particles is not accounted for, the onset of $\ell = 0$ instability does not necessarily lead to an explosion (Appendix A), thus the instability thresholds do not equal explosion criteria for the parametric setup.

Our results show that despite the non-linearity of the flow, clear signatures of the operation of the SASI and convection can be obtained. In particular, the parameter χ (equation 6) – evaluated at the time where the shock stalls and before hydrodynamic instabilities set in – is a good predictor of whether the system will be SASI- or convection-dominated on its way to explosion.

Despite the different explosion paths obtained when SASI or convection dominate the dynamics at early times, it is not clear that the resulting explosion properties are very different once the process has started. Our results indicate that in both cases, the formation of at least one large-scale, high-entropy bubble is a necessary condition to achieve explosion in two-dimensions. It may be that this degeneracy is triggered by the inverse turbulent cascade inherent in axisymmetric models.

The absence of this inverse cascade in 3D causes the flow to develop more small-scale structure than in 2D (e.g., Hanke et al. 2012). Nonetheless, the tendency of bubbles to merge into bigger structures will persist, as this is an intrinsic property of the Rayleigh-Taylor instability (Sharp 1984).

In fact, several 3D hydrodynamic studies have observed that prior to explosion, a large-scale asymmetry (often $\ell = 1$) develops in a non-oscillatory way (Iwakami et al. 2008; Couch 2013a; Dolence et al. 2013; Hanke et al. 2013). The difference lies in the fact that the SASI provides seeds for large-scale entropy fluctuations *independent of dimension*, so it can speed up the formation of a large- and hot enough bubble to achieve explosion. Verifying whether this picture is robust requires numerical experiments in 3D.

Even though we have found clear evidence for high entropy bubbles playing a key role in the interplay between SASI and convection and in the onset of explosion, there are many questions that remain to be answered. First, the evolution of the f_V diagnostic suggests that transition to explosion in a multidimensional environment involves a fraction of the gain region volume achieving a certain entropy or positive energy. What is that volume or mass fraction, and what are the required entropy or energy values as a function of the dominant system parameters?

Second, our characterization of large bubble dynamics in the gain region is limited. Processes such as seeding of bubbles by shock displacements, survivability of bubbles due to neutrino heating, buoyancy, and the turbulent cascade, disruption by lateral SASI flows in the linear phase or low-entropy plumes in the non-linear phase, and feedback of these bubbles on SASI modes deserve further study. Preliminary steps in this direction have already been taken (e.g., Guilet et al. 2010; Couch 2013a; Dolence et al. 2013; Murphy et al. 2013), though much more work remains if a quantitative understanding – in the form of a predictive explosion criterion – is to be attained.

It is interesting to compare the critical heating rates for explosion in our parametric models and those from light-bulb setups with a full EOS and a time-dependent mass accretion rate (e.g., Nordhaus et al. 2010; Hanke et al. 2012; Couch 2013a). In the former, explosion occurs above (but close to) the $\ell = 0$ instability threshold in both SASI- and convection-dominated models, with only a $\sim 10\%$ difference between 1D and 2D (Fig. 1). In contrast, the latter models are such that non-spherical instabilities make a larger difference ($\sim 20\%$) relative to the 1D case, with explosion occurring for heating rates below the $\ell = 0$ oscillatory instability. Note however that both classes of models neglect the (negative) feedback to the heating rate due to the drop in accretion luminosity when the shock expands, thus the numbers obtained from these models should be treated with caution. The search for a robust and predictive explosion criterion valid for both SASI- and convection-dominated models is a worthwhile pursuit, though outside the scope of the present paper.

The modification of our results by the introduction of a third spatial dimension will be addressed in future work.

APPENDIX A: ON THE STABILITY OF THE $\ell = 0$ SASI MODE

Here we compare the predictions from timescale ratio diagnostics with the actual eigenfrequencies of the $\ell = 0$ mode in the parametric system.

Figure A1 shows the shock radius as a function of time for one dimensional (1D) versions of the e0 and e3 sequences shown in Table 1. By comparing with Figure 1, one can see that the oscillatory radial stability thresholds are well captured at this resolution. The initial value of the ratio of advection time in the gain region to advection time in the cooling region is a good indicator of oscillatory radial stability for the $\varepsilon = 0$ sequence, but not so much when nuclear dissociation is introduced.

The initial ratio of advection to heating times in the gain region is a good predictor of non-oscillatory expansion in the 1D models, in agreement with the numerical results of Fernández (2012). Note however that for both sequences, this point lies at a lower heating rate than the bifurcation of the perturbative $\ell = 0$ growth rate (Fig. 1). Therefore, this runaway expansion is a non-linear effect, likely arising from the fact that the growth time is shorter than the oscillation period (by more than a factor of two in the e0 model when the ratio of advection to heating timescales is unity).

Note also that in contrast to the models of Fernández (2012), radial instability does not always lead to runaway expansion. This is clear from the model with $\varepsilon = 0$ and $B = 0.01$, which saturates. Also, all the models with nuclear dissociation saturate. Fernández & Thompson (2009a) showed that this effect is due to the artificial assumption of constant nuclear dissociation at the shock. Including the recombination energy of alpha particles as the shock expands (which decreases the effective dissociation rate), leads to a runaway as soon as instability sets in.
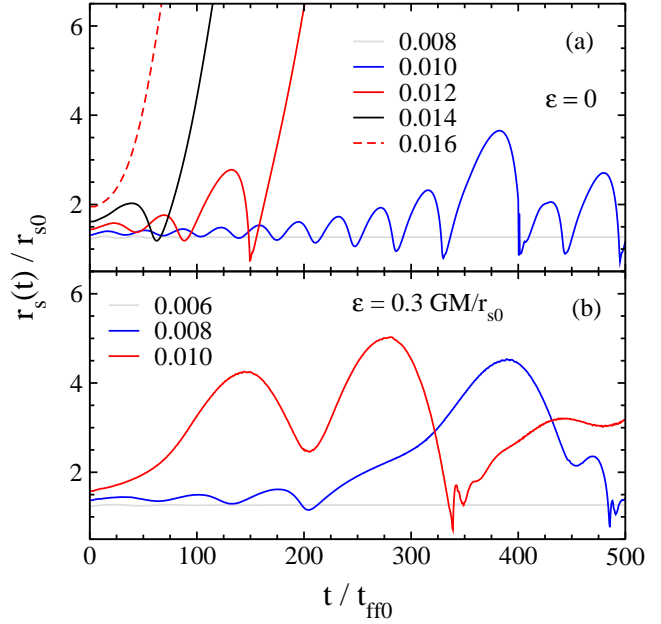

Figure A1. Shock radius as a function of time for 1D models without dissociation (panel a) and with dissociation (panel b). Curves are labeled by the value of the heating parameter B; compare with Figure 1. Note that non-oscillatory expansion sets in when B is such that $t_{\text{adv}-\text{g}} > t_{\text{heat}-\text{g}}$. The shock expansion saturates in all models with dissociation, and in the model with $B = 0.01$ and $\varepsilon = 0$.

APPENDIX B: SPHERICAL FOURIER-BESSEL DECOMPOSITION IN BETWEEN CONCENTRIC SHELLS

In spherical polar coordinates, the general solution to the Helmholtz equation[4] is a superposition of functions of the form (e.g., Jackson 1999)

$$[a_{\ell,m} j_\ell(kr) + b_{\ell,m} y_\ell(kr)] Y_\ell^m(\theta, \phi), \quad (B1)$$

where j_ℓ and y_ℓ are the spherical Bessel functions, Y_ℓ^m are the Laplace spherical harmonics, and $\{a_{\ell,m}, b_{\ell,m}\}$ are constant coefficients. The wavenumber k and the coefficients are determined once boundary conditions for the problem are imposed at the radial domain boundaries r_{in} and r_{out}.

B1   Dirichlet Boundary Conditions

Requiring that the eigenfunctions vanish at the radial boundaries for all $\{\ell, m\}$ yields the system of equations

$$\begin{bmatrix} j_\ell(k\, r_{\text{in}}) & y_\ell(k\, r_{\text{in}}) \\ j_\ell(k\, r_{\text{out}}) & y_\ell(k\, r_{\text{out}}) \end{bmatrix} \begin{pmatrix} a_{\ell,m} \\ b_{\ell,m} \end{pmatrix} = 0. \quad (B2)$$

Non-trivial solutions are obtained by setting the determinant of the matrix of coefficients to zero. This condition then defines a discrete set of radial wavenumbers:

$$j_\ell(k_{n\ell}\, r_{\text{in}})\, y_\ell(k_{n\ell}\, r_{\text{out}}) - j_\ell(k_{n\ell}\, r_{\text{out}})\, y_\ell(k_{n\ell}\, r_{\text{in}}) = 0 \quad (B3)$$
$$(n = 0, 1, 2, ...)$$

---

[4] Since the Laplacian operator is Hermitian, its eigenfunctions – solutions to the Helmholtz equation – form a complete orthogonal basis in the Hilbert space L^2 (Arfken & Weber 2005).
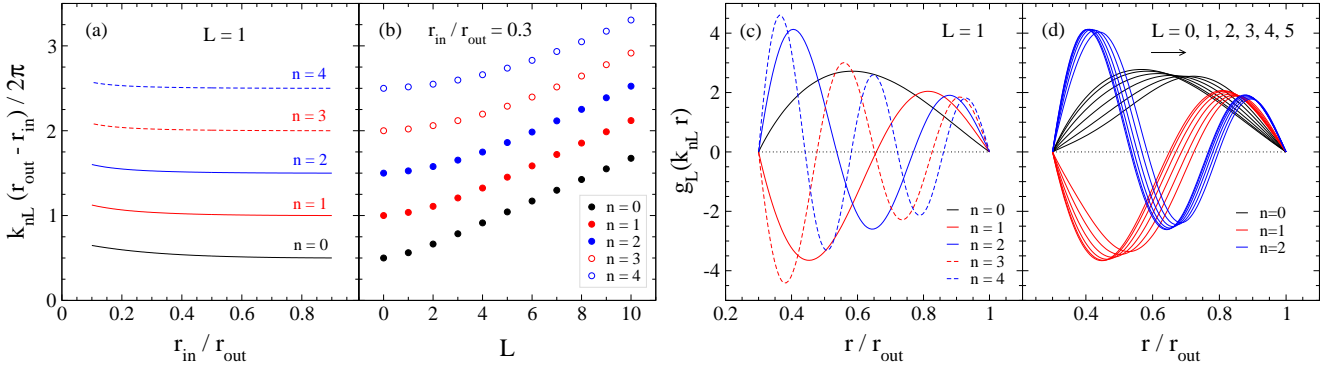
Figure B1. Properties of the radial eigenfunctions for Dirichlet boundary conditions. Panel (a) shows wave numbers corresponding to the fundamental and first four harmonics as a function of the domain size, for $\ell = 1$. Panel (b) shows the corresponding wave numbers when varying ℓ, for fixed $r_{\rm in}/r_{\rm out} = 0.3$. Panel (c) shows normalized eigenfunctions as a function of radius, for the fundamental and the first four harmonics of $\ell = 1$ and $r_{\rm in}/r_{\rm out} = 0.3$. Panel (d) shows the effect of varying ℓ from 0 to 5 on the fundamental and first two overtones, for the same domain size as panel (c). Higher ℓ values shift curves to the right.
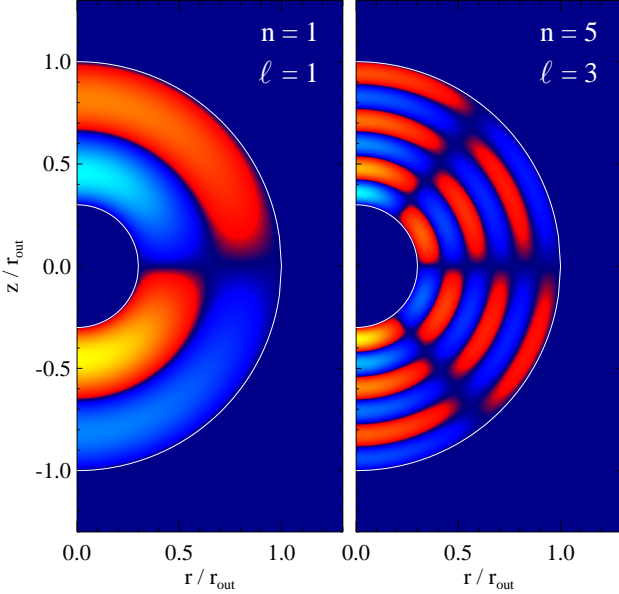

Figure B2. Examples of spherical Fourier-Bessel basis functions in two dimensions (r, θ), for a ratio of radii $r_{\rm in}/r_{\rm out} = 0.3$. Parameters are $\{n = 1, \ell = 1\}$ (left) and $\{n = 5, \ell = 3\}$ (right). The basis functions vanish at the radial boundaries.

where n labels the roots in increasing magnitude.

Figure B1a shows the first five solutions for $\ell = 1$, as a function of the ratio of boundary radii $r_{\rm in}/r_{\rm out}$. We adopt the convention of labeling the smallest wavenumber by $n = 0$, since the eigenfunction has no nodes. For low ℓ, the relation

$$k_{n\ell} \simeq \frac{\pi}{(r_{\rm out} - r_{\rm in})}(n + 1) \qquad n = 0, 1, 2... \tag{B4}$$

holds approximately, becoming better for $r_{\rm in}/r_{\rm out} \to 1$. Increasing the angular degree increases the value of the wave number relative to equation (B4), as shown in Figure B1b.

Equation (B2) also determines the ratio of coefficients

$$\frac{b_{n\ell m}}{a_{n\ell m}} = -\frac{j_\ell(k_{n\ell} r_{\rm in})}{y_\ell(k_{n\ell} r_{\rm in})} = -\frac{j_\ell(k_{n\ell} r_{\rm out})}{y_\ell(k_{n\ell} r_{\rm out})}. \tag{B5}$$

Note that n has been added as an index to the coefficients. The radial eigenfunctions g_ℓ are then

$$
\begin{aligned}
g_{n\ell}(r) &= N_{n\ell}^{-1/2} \left[y_\ell(k_{n\ell} r_{\rm out}) j_\ell(k_{n\ell} r) \right. \\
&\quad \left. - j_\ell(k_{n\ell} r_{\rm out}) y_\ell(k_{n\ell} r) \right] \tag{B6} \\
&= \tilde{N}_{n\ell}^{-1/2} \left[y_\ell(k_{n\ell} r_{\rm in}) j_\ell(k_{n\ell} r) \right. \\
&\quad \left. - j_\ell(k_{n\ell} r_{\rm in}) y_\ell(k_{n\ell} r) \right], \tag{B7}
\end{aligned}
$$

where the two formulations differ only by a global (real) phase. The normalization constant is found from the orthogonality condition (Lommel integral). Combining two solutions of the spherical Bessel differential equation, integrating over the radial domain, applying the boundary conditions, and using L'Hôpital's rule yields

$$
\int_{r_{\rm in}}^{r_{\rm out}} g_\ell(k_{n\ell} r) g_\ell(k_{m\ell} r)\, r^2 {\rm d}r = \frac{\delta_{nm}}{2} \left\{ r_{\rm out}^3 \left[g_\ell'(k_{n\ell} r_{\rm out}) \right]^2 \right.
$$
$$
\left. - r_{\rm in}^3 \left[g_\ell'(k_{n\ell} r_{\rm in}) \right]^2 \right\}, \tag{B8}
$$

where δ_{nm} is the Kronecker symbol and primes denote derivative respect to the argument. For the first formulation (eq. B6), choosing

$$
\begin{aligned}
N_{n\ell} &= \frac{1}{2} \left\{ r_{\rm out}^3 \left[y_\ell(k_{n\ell} r_{\rm out}) j_\ell'(k_{n\ell} r_{\rm out}) \right. \right. \\
&\quad \left. - j_\ell(k_{n\ell} r_{\rm out}) y_\ell'(k_{n\ell} r_{\rm out}) \right]^2 \\
&\quad - r_{\rm in}^3 \left[y_\ell(k_{n\ell} r_{\rm out}) j_\ell'(k_{n\ell} r_{\rm in}) \right. \\
&\quad \left. \left. - j_\ell(k_{n\ell} r_{\rm out}) y_\ell'(k_{n\ell} r_{\rm in}) \right]^2 \right\} \tag{B9}
\end{aligned}
$$

makes the eigenfunctions orthonormal. Figure B2 shows two examples of the resulting normalized eigenfunctions in a two dimensional, axisymmetric space.

In three dimensions, the expansion of an arbitrary function $f(r, \theta\, \phi)$ with Dirichlet boundary conditions in the radial interval $[r_{\rm in}, r_{\rm out}]$ can be written as

$$f(r, \theta, \phi) = \sum_{n, \ell, m} f_{n\ell m} g_\ell(k_{n\ell} r) Y_\ell^m(\theta, \phi), \tag{B10}$$

with coefficients given by

$$f_{n\ell m} = \int r^2 {\rm d}r\, {\rm d}\Omega\, g_\ell(k_{n\ell} r) Y_\ell^{m*} F(r, \theta, \phi), \tag{B11}$$
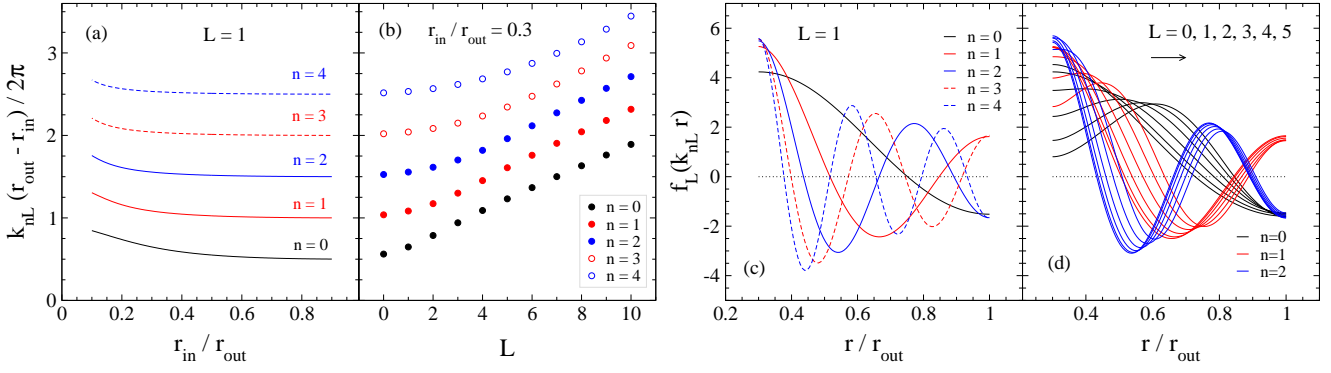
Figure B3. Same as Figure B1, but for Neumann boundary conditions.

where the star denotes complex conjugation. The corresponding Parseval identity is

$$\int |F| \, \mathrm{d}^3 x = \sum_{n,\ell,m} |a_{n\ell m}|^2 \tag{B12}$$

yielding a three-dimensional spatial power spectrum:

$$P_{n\ell m} = |a_{n\ell m}|^2. \tag{B13}$$

B2 Neumann Boundary Conditions

Requiring that the radial derivative of the eigenfunctions vanish at the boundaries yields the equation for the radial wave numbers

$$j'_\ell(k_n \, r_{\mathrm{in}}) \, y'_\ell(k_n \, r_{\mathrm{out}}) - j'_\ell(k_n \, r_{\mathrm{out}}) \, y'_\ell(k_n \, r_{\mathrm{in}}) = 0 \tag{B14}$$
$$(n = 1, 2, 3...),$$

where the primes again denote derivative respect to the argument. The eigenfunctions are now

$$\begin{aligned}
f_\ell(k_n \, r) &= M^{-1/2} \left[y'_\ell(k_n \, r_{\mathrm{in}}) j_\ell(k_n \, r) \right. \\
&\quad \left. - j'_\ell(k_n \, r_{\mathrm{in}}) y_\ell(k_n \, r) \right] \tag{B15} \\
&= \tilde{M}^{1/2} \left[y'_\ell(k_n \, r_{\mathrm{out}}) j_\ell(k_n \, r) \right. \\
&\quad \left. - j'_\ell(k_n \, r_{\mathrm{out}}) y_\ell(k_n \, r) \right], \tag{B16}
\end{aligned}$$

and the orthogonality condition reads

$$\int_{r_{\mathrm{in}}}^{r_{\mathrm{out}}} f_\ell(k_n \, r) f_\ell(k_m \, r) \, r^2 \mathrm{d}r =$$
$$\frac{\delta_{nm}}{2} \left\{ r_{\mathrm{out}}^3 \left[1 - \frac{\ell(\ell+1)}{(k_{n\ell} r_{\mathrm{out}})^2} \right] f_\ell^2(k_{n\ell} \, r_{\mathrm{out}}) \right.$$
$$\left. - r_{\mathrm{in}}^3 \left[1 - \frac{\ell(\ell+1)}{(k_{n\ell} r_{\mathrm{in}})^2} \right] f_\ell^2(k_{n\ell} \, r_{\mathrm{in}}) \right\}. \tag{B17}$$

The normalization constant for equation (B15) is

$$\begin{aligned}
M_{n\ell} &= \frac{1}{2} \left\{ r_{\mathrm{out}}^3 \left[1 - \frac{\ell(\ell+1)}{(k_{n\ell} r_{\mathrm{out}})^2} \right] \times \right. \\
&\quad \left[y'_\ell(k_{n\ell} r_{\mathrm{out}}) \, j_\ell(k_{n\ell} r_{\mathrm{out}}) - j'_\ell(k_{n\ell} r_{\mathrm{out}}) \, y_\ell(k_{n\ell} r_{\mathrm{out}}) \right]^2 \\
&\quad - r_{\mathrm{in}}^3 \left[1 - \frac{\ell(\ell+1)}{(k_{n\ell} r_{\mathrm{in}})^2} \right] \left[y'_\ell(k_{n\ell} r_{\mathrm{out}}) \, j_\ell(k_{n\ell} r_{\mathrm{in}}) \right. \\
&\quad \left. \left. - j'_\ell(k_{n\ell} r_{\mathrm{out}}) \, y_\ell(k_{n\ell} r_{\mathrm{in}}) \right]^2 . \right\} \tag{B18}
\end{aligned}$$

The radial wave numbers and eigenfunctions for the first few harmonics and ℓ values are shown in Figure B3.

The overall structure of the wave numbers is very similar to the Dirichlet case, with slightly higher values for small ratio of radii and large ℓ. For fixed harmonic, the eigenfunctions change their shape as ℓ is increased, in contrast to the Dirichlet case.

REFERENCES

Arfken G. B., Weber H. J., 2005, Mathematical Methods for Physicists, sixth edn. Elsevier, Amsterdam
Arnett W. D., Meakin C., 2011, ApJ, 733, 78
Bethe H. A., 1990, Reviews of Modern Physics, 62, 801
Bethe H. A., Wilson J. R., 1985, ApJ, 295, 14
Blondin J. M., Mezzacappa A., 2006, ApJ, 642, 401
Blondin J. M., Mezzacappa A., 2007, Nature, 445, 58
Blondin J. M., Mezzacappa A., DeMarino C., 2003, ApJ, 584, 971
Blondin J. M., Shaw S., 2007, ApJ, 656, 366
Bruenn S. W., Dirk C. J., Mezzacappa A., Hayes J. C., Blondin J. M., Hix W. R., Messer O. E. B., 2006, Journal of Physics Conference Series, 46, 393
Buras R., Janka H.-T., Rampp M., Kifonidis K., 2006, A&A, 457, 281
Buras R., Rampp M., Janka H.-T., Kifonidis K., 2006, A&A, 447, 1049
Burrows A., 2013, RMP, 85, 245
Burrows A., Dolence J. C., Murphy J. W., 2012, ApJ, 759, 5
Burrows A., Hayes J., Fryxell B. A., 1995, ApJ, 450, 830
Burrows A., Livne E., Dessart L., Ott C. D., Murphy J., 2007, ApJ, 655, 416
Ciaraldi-Schoolmann F., Schmidt W., Niemeyer J. C., Röpke F. K., Hillebrandt W., 2009, ApJ, 696, 1491
Couch S. M., 2013a, ApJ, 775, 35
Couch S. M., 2013b, ApJ, 765, 29
Couch S. M., Ott C. D., 2013, ApJL, submitted, arXiv:1309.2632
Davidson P. A., 2004, Turbulence: an introduction for scientists and engineers, first edn. Oxford University Press, Oxford
Dolence J. C., Burrows A., Murphy J. W., Nordhaus J., 2013, ApJ, 765, 110
Dubey A., Antypas K., Ganapathy M. K., Reid L. B., Riley K., Sheeler D., Siegel A., Weide K., 2009, J. Par. Comp., 35, 512

Endeve E., Cardall C. Y., Budiardja R. D., Beck S. W., Bejnood A., Toedte R. J., Mezzacappa A., Blondin J. M., 2012, ApJ, 751, 26

Fernández R., 2010, ApJ, 725, 1563

Fernández R., 2012, ApJ, 749, 142

Fernández R., Thompson C., 2009a, ApJ, 703, 1464

Fernández R., Thompson C., 2009b, ApJ, 697, 1827

Fisher K. B., Lahav O., Hoffman Y., Lynden-Bell D., Zaroubi S., 1995, MNRAS, 272, 885

Foglizzo T., 2009, ApJ, 694, 820

Foglizzo T., Galletti P., Scheck L., Janka H.-T., 2007, ApJ, 654, 1006

Foglizzo T., Scheck L., Janka H.-T., 2006, ApJ, 652, 1436

Fryer C. L., Young P. A., 2007, ApJ, 659, 1438

Guilet J., Foglizzo T., 2012, MNRAS, 421, 546

Guilet J., Sato J., Foglizzo T., 2010, ApJ, 713, 1350

Hammer N. J., Janka H.-T., Müller E., 2010, ApJ, 714, 1371

Hanke F., Marek A., Müller B., Janka H.-T., 2012, ApJ, 755, 138

Hanke F., Müller B., Wongwathanarat A., Marek A., Janka H.-T., 2013, ApJ, 770, 66

Herant M., Benz W., Hix W. R., Fryer C. L., Colgate S. A., 1994, ApJ, 435, 339

Iwakami W., Kotake K., Ohnishi N., Yamada S., Sawada K., 2008, ApJ, 678, 1207

Jackson J. D., 1999, Classical Electrodynamics, third edn. Wiley, Hoboken

Janka H.-T., 2001, A&A, 368, 527

Janka H.-T., 2012, Ann. Rev. Nuc. Part. Sci., 62, 407

Janka H.-T., Hanke F., Hüdepohl L., Marek A., Müller B., Obergaulinger M., 2012, Prog. Th. Ex. Phys., 2012, 010000

Janka H.-T., Keil W., 1998, in L. Labhardt, B. Binggeli, & R. Buser ed., Supernovae and cosmology Perspectives of Core-Collapse Supernovae beyond SN 1987A. p. 7

Janka H.-T., Müller E., 1996, A&A, 306, 167

Kifonidis K., Plewa T., Scheck L., Janka H.-T., Müller E., 2006, A&A, 453, 661

Kraichnan R. H., 1967, Physics of Fluids, 10, 1417

Marek A., Janka H.-T., 2009, ApJ, 694, 664

Mezzacappa A., Calder A. C., Bruenn S. W., Blondin J. M., Guidry M. W., Strayer M. R., Umar A. S., 1998, ApJ, 495, 911

Müller B., Janka H.-T., Dimmelmeier H., 2010, ApJS, 189, 104

Müller B., Janka H.-T., Heger A., 2012, ApJ, 761, 72

Müller B., Janka H.-T., Marek A., 2013, ApJ, 766, 43

Müller E., Janka H.-T., Wongwathanarat A., 2012, A&A, 537, 63

Murphy J. W., Burrows A., 2008, ApJ, 688, 1159

Murphy J. W., Dolence J. C., Burrows A., 2013, ApJ, 771, 52

Murphy J. W., Meakin C., 2011, ApJ, 742, 74

Niemeyer J. C., Woosley S. E., 1997, ApJ, 475, 740

Nordhaus J., Brandt T. D., Burrows A., Livne E., Ott C. D., 2010, PRD, 82, 103016

Nordhaus J., Burrows A., Almgren A., Bell J., 2010, ApJ, 720, 694

Ohnishi N., Kotake K., Yamada S., 2006, ApJ, 641, 1018

Ott C. D., Burrows A., Dessart L., Livne E., 2008, ApJ, 685, 1069

Ott C. D., et al., 2013, ApJ, 768, 115

Press W. H., Teukolski S. A., Vetterling W. T., Flannery B. P., 2006, Numerical Recipes in Fortran 77, second edn. Cambridge University Press, Cambridge

Rampp M., Janka H.-T., 2002, A&A, 396, 361

Scheck L., Janka H.-T., Foglizzo T., Kifonidis K., 2008, A&A, 477, 931

Scheck L., Kifonidis K., Janka H.-T., Müller E., 2006, A&A, 457, 963

Sharp D. H., 1984, Physica D Nonlinear Phenomena, 12, 3

Suwa Y., Kotake K., Takiwaki T., Whitehouse S. C., Liebendörfer M., Sato K., 2010, PASJ, 62, L49

Takiwaki T., Kotake K., Suwa Y., 2012, ApJ, 749, 98

Thompson C., 2000, ApJ, 534, 915

Thompson T. A., Quataert E., Burrows A., 2005, ApJ, 620, 861

Wongwathanarat A., Janka H.-T., Müller E., 2010, ApJ, 725, L106

Wongwathanarat A., Janka H.-T., Müller E., 2013, A&A, 552, 126

Woosley S. E., Heger A., Weaver T. A., 2002, Reviews of Modern Physics, 74, 1015

Yamasaki T., Yamada S., 2007, ApJ, 656, 1019